

Redshift Space Distortion of the 21cm Background from the Epoch of Reionization I: Methodology Re-examined

Yi Mao,^{1*} Paul R. Shapiro,^{1†} Garrelt Mellema,² Ilian T. Iliev,³ Jun Koda,¹
and Kyungjin Ahn⁴

¹ Department of Astronomy and Texas Cosmology Center, University of Texas, Austin, TX 78712, USA

² Department of Astronomy & Oskar Klein Centre, AlbaNova, Stockholm University, SE-106 91 Stockholm, Sweden

³ Astronomy Centre, Department of Physics & Astronomy, Pevensey II Building, University of Sussex, Falmer, Brighton BN1 9QH, UK

⁴ Department of Earth Science Education, Chosun University, Gwangju 501-759, Korea

Released 31 October 2018

ABSTRACT

The peculiar velocity of the intergalactic gas responsible for the cosmic 21cm background from the epoch of reionization (EOR) and beyond introduces an anisotropy in the three-dimensional power spectrum of brightness temperature fluctuations. Measurement of this anisotropy by future 21cm surveys is a promising tool for separating cosmology from 21cm astrophysics. A more careful treatment of the effects of peculiar velocity than previously attempted is necessary, however, to fulfill this promise. This paper sets out to account for peculiar velocity in every detail. We begin by re-deriving the brightness temperature dependence on atomic hydrogen density, spin temperature, peculiar velocity and its gradient, and redshift, to clarify the roles of thermal vs. velocity broadening and finite optical depth. The observed 21cm maps can be distorted, not only because the apparent location inferred from the line-frequency shift is distorted by peculiar velocity, but also because the brightness temperature, itself, depends on that velocity and its gradient. We show that even the *angle-averaged* power spectrum, $P(k)$, is affected significantly by peculiar velocity.

To facilitate the prediction of the observed 21cm background from large-scale N-body and radiative-transfer simulations of reionization, we propose two numerical schemes to incorporate peculiar velocity accurately, one particle-based, one grid-based, both involving real-to redshift-space re-mapping of the H I density. We show how the grid-based scheme can be optimized for accuracy and computational efficiency. We use these results to show that previous treatment of the velocity-gradient correction to 21cm brightness temperature in real space can result in significant errors in power spectrum on all scales.

Key words: Cosmology: theory–reionization– physical data and processes: radiative transfer– methods: analytical–numerical– galaxies: intergalactic medium

1 INTRODUCTION

Neutral hydrogen atoms in the intergalactic medium (IGM) at high redshift contribute a diffuse background of redshifted 21cm radiation which encodes information about the physical conditions in the early universe during and before the epoch of reionization (EOR, $z > 6$). Three-dimensional mapping of this 21cm background (a.k.a. 21cm tomography) has recently been proposed as a promising cosmological probe. In principle, it has greater potential than the cosmic microwave background (CMB) since it can map most of our horizon volume thus providing unprecedented cosmological information (Mao et al. 2008). The precision with which

21cm tomography can constrain cosmological parameters has been forecast in several studies. Some of these consider mapping diffuse hydrogen in the IGM before and during the EOR (McQuinn et al. 2006; Bowman, Morales & Hewitt 2007; Santos & Cooray 2006; Mao et al. 2008; Barger et al. 2009; Adshead et al. 2011), others mapping neutral hydrogen in galactic halos after reionization (Wyithe, Loeb & Geil 2008; Visbal, Loeb & Wyithe 2009). These studies show that cosmological constraints based on CMB measurements can be significantly improved if combined with 21cm measurements.

The next few decades promise to become a golden age for 21cm tomography, with about a half-dozen experiments already proposed or underway for measuring the 21cm background from

* Email: ymao@astro.as.utexas.edu

† Email: shapiro@astro.as.utexas.edu

the EOR, including the upcoming first generation such as 21CMA¹, MWA², LOFAR³, GMRT⁴, and PAPER⁵, and the next generation such as SKA⁶ (under plan), and the *Omniscope*⁷ (proposed by Tegmark & Zaldarriaga 2009, 2010). These telescopes will measure the 21cm signal either statistically (first generation telescopes) or by precise imaging and map making (next generation telescopes).

All observations will give the redshifted 21cm signal in observer redshift-space, where the frequency not only depends on the cosmological redshift, but also on the peculiar velocity of the IGM. However, most theoretical endeavors, both in analytical modelling (e.g., Furlanetto, Zaldarriaga & Hernquist 2004; Iliev et al. 2002), semi-numerical (e.g., Alvarez et al. 2009; Zahn et al. 2007, 2010) and in numerical simulations (e.g., Shapiro et al. 2006, 2008, Iliev et al. 2006, 2008a; McQuinn et al. 2007; Trac & Cen 2007), have focused on predicting the 21cm signal without taking peculiar velocities into account.

In the linear regime, the effects of peculiar velocities have been studied analytically by Bharadwaj, Nath & Sethi (2001), Bharadwaj & Ali (2004), Barkana & Loeb (2005) and Wang & Hu (2006). In this regime, it has been shown, it is possible to separate the contributions to the brightness temperature fluctuation statistics from the patchiness of reionization and the cosmological density fluctuations, respectively (Barkana & Loeb 2005). This, it is hoped, would make it possible to use 21cm measurements to solve for cosmological parameters. However, the *nonlinear* 21cm redshift-space-distortion effect remains largely unexplored⁸ and may spoil these well-understood linear theory predictions at intermediate scales.

Given the rapid progress of observations (e.g., GMRT has placed an upper bound on the 21cm power spectrum at $z \approx 8.6$ in their first result release [Paciga et al. 2010], and MWA and LOFAR are close to their data collection stage), we urgently need a thorough understanding of how peculiar velocities enter into predictions of the 21cm signal in observer redshift-space from results of modelling or simulations in real space.

Along these lines, Mellema et al. (2006b, their Figs. 4, 9 and 10) were the first to consider the effect of peculiar velocities on the 21cm brightness temperature fluctuations in observer redshift-space when making spectra and maps along the line of sight (LOS). They found significant differences between maps and spectra of brightness temperature with and without the effects of peculiar velocities. However, they did not account for this effect when calculating statistical properties such as the power spectra of the brightness temperature fluctuations, nor did they explain in detail how the effects of peculiar velocities were implemented. Thomas et al. (2009) claimed to include the effects of peculiar velocities without presenting any details on how these were calculated nor any analysis of the effects. More recently, Santos et al. (2010) proposed an

approximate scheme, also adopted by Mesinger, Furlanetto & Cen (2011), to compute the 21cm power spectrum in redshift space in semi-numerical models of the evolving IGM. The accuracy of their approximation, especially with regard to treatment of the divergences which result when correcting the brightness temperature for peculiar velocity in real space, has not yet been determined. We shall investigate this below.

Our paper is the first in a series which sets out to build a solid and self-consistent computational scheme to predict the 21cm background accurately in observer redshift space, given density, velocity and ionization fraction information in real space. The second paper (Shapiro et al. 2011) of this series will focus on the nonlinear effects of inhomogeneous reionization coupled to peculiar velocity, and test the validity of using the 21cm background for cosmology. Some of our results were previously summarized by us in Mao et al. (2010).

This paper is organized as follows. In Section 2, we will demonstrate how important the effects of peculiar velocity are by comparing the angle-averaged power spectra of brightness temperature fluctuations calculated from reionization simulations in two different ways, using linear theory which takes peculiar velocity into account and using the simulation data without peculiar velocity, respectively. We then clarify our terminology in Section 3. In Section 4, we use a heuristic derivation to present a simple picture of redshift-space distortions of the 21cm background in the limit of low optical depth and high spin temperature, and clarify the similarities and differences with galaxy redshift surveys. In Section 5, we re-derive the 21cm *observed* brightness temperature by solving the radiative transfer equation for 21cm radiation, accounting for all possible contributions of peculiar velocity to the order $\mathcal{O}(v/c)$. Next we lay the theoretical foundations of calculating the 21cm redshift-space-distorted brightness temperature from real-space data. In Section 6, we propose two computational schemes, one based on particle data and one based on grid data. We test these schemes and find an empirical condition for the accuracy of the grid-based scheme. In Section 7, we evaluate the approximate “velocity-gradient-limited” prescription proposed by Santos et al. (2010) and show its shortcomings. We compare the usability, accuracy and efficiency of our different schemes in Section 8, and conclude in Section 9. We include some technical details of post-processing massive numerical particle data in Appendix A.

2 HOW IMPORTANT IS PECULIAR VELOCITY?

Before developing our methodologies we will illustrate the effects of peculiar velocities on the 21cm power spectrum as measured in redshift-space, to show their importance. For this purpose, we focus on the limiting case in which the spin temperature greatly exceeds the CMB temperature and the optical depth is small, so we can write the differential brightness temperature, $\delta T_b \equiv T_b - T_{\text{CMB}}$, as follows:

$$\delta T_b(\nu_{\text{obs}}) = \widehat{\delta T}_b(z_{\text{cos}}) \frac{1 + \delta_{\rho_{\text{HI}}}^r(\mathbf{r})}{|1 + \delta_{\partial_r v}(\mathbf{r})|}, \quad (1)$$

where the pre-factor $\widehat{\delta T}_b$ is the cosmic mean value in this limit and will be defined in Eqn. (35). Here z_{cos} is the cosmological redshift, \mathbf{r} is the comoving real-space coordinates, and $\delta_{\rho_{\text{HI}}}^r$ and $\delta_{\rho_{\text{H}}}^r$ are the fluctuations of neutral and total hydrogen density in real space, respectively; i.e. $\rho_{\text{HI}} = \rho_{\text{H}} x_{\text{HI}}$, and $\delta_{\rho_{\text{HI}}}^r = \delta_{\rho_{\text{H}}}^r + \delta_{x_{\text{HI}}}^r + \delta_{\rho_{\text{H}}}^r \delta_{x_{\text{HI}}}^r$, where x_{HI} is neutral fraction of hydrogen atoms. Also, we define

¹ <http://21cma.bao.ac.cn/>

² <http://www.haystack.mit.edu/ast/arrays/mwa/>

³ <http://www.lofar.org>

⁴ <http://gmrt.ncra.tifr.res.in>

⁵ <http://astro.berkeley.edu/~dbacker/eor/>

⁶ <http://www.skatelescope.org>

⁷ http://en.wikipedia.org/wiki/Fast_Fourier_Transform_Telescope, formerly termed *Fast Fourier Transform Telescope*.

⁸ Shaw & Lewis (2008) presented a nonlinear analysis for the redshift-space distortion. However, they assumed the 21cm brightness temperature fluctuations are Gaussian, which may not be valid for the EOR (see, e.g. Fig. 14 of Mellema et al. 2006b).

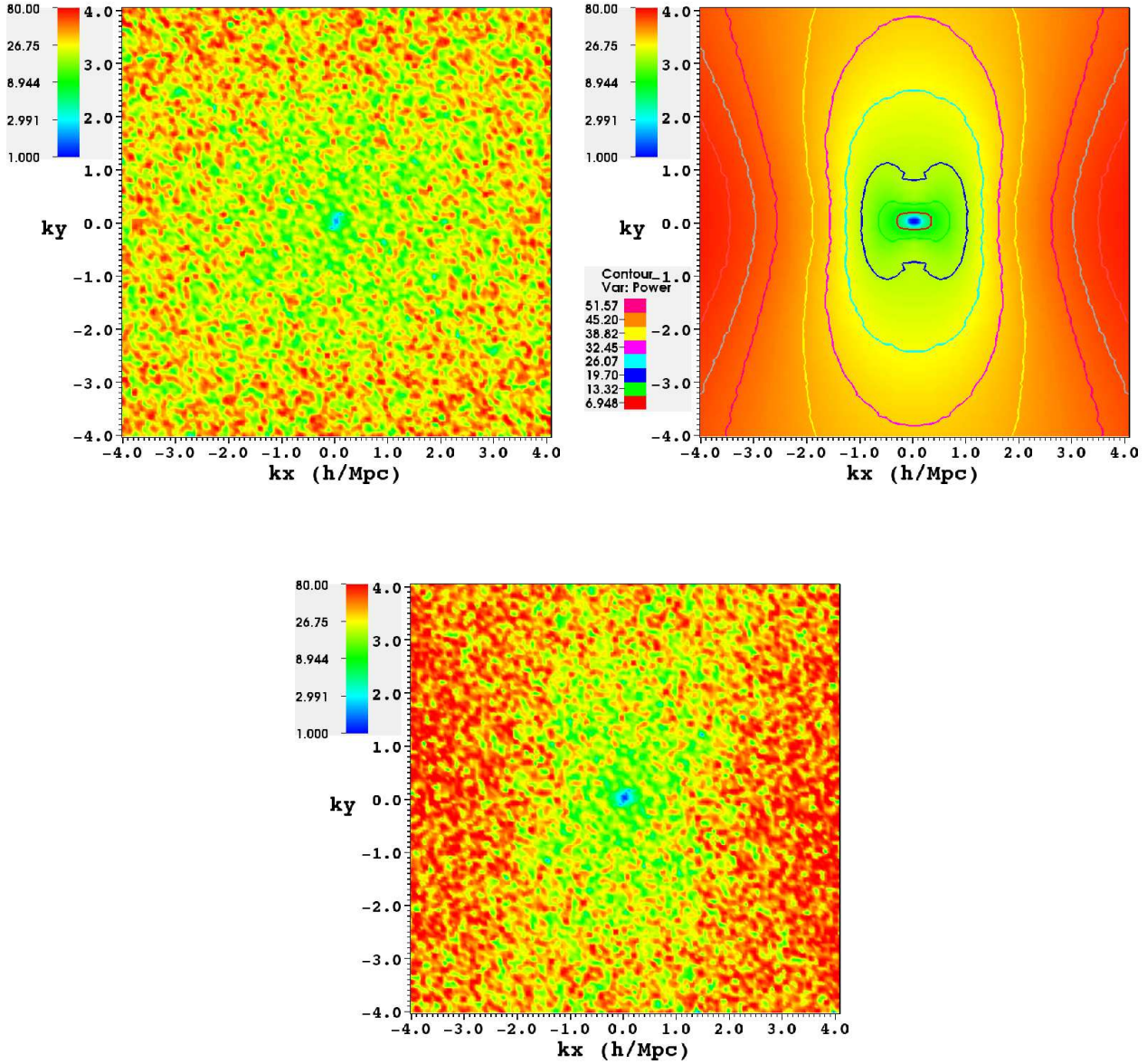


Figure 1. 3D power spectra $\Delta^2(\mathbf{k}) \equiv k^3 P_{21}(\mathbf{k})/2\pi^2$ (in units of mK^2) of 21cm brightness temperature fluctuations. The panels show a slice through the k_x - k_y plane, with the LOS along the x -axis, calculated from our numerical simulation at the 50% ionized epoch ($z = 9.457$). Top left: UPV scheme; top right: linear $\mu_{\mathbf{k}}$ -decomposition scheme; bottom: the fully nonlinear PPM-RRM scheme.

the quantity

$$\delta_{\partial_r v}(\mathbf{r}) \equiv \frac{1 + z_{\text{cos}}}{H(z_{\text{cos}})} \frac{dv_{\parallel}}{dr_{\parallel}}(\mathbf{r}), \quad (2)$$

the gradient of the proper radial peculiar velocity along the LOS, normalized by the conformal Hubble constant $H/(1 + z_{\text{cos}})$. The power spectrum of brightness temperature fluctuations in observer redshift-space can then be written as $\langle \widehat{\delta T_b^*}(\mathbf{k}) \widehat{\delta T_b}(\mathbf{k}') \rangle \equiv (2\pi)^3 P_{\Delta T}^{3D}(\mathbf{k}) \delta^{(3)}(\mathbf{k} - \mathbf{k}')$, where $\widehat{\delta T_b}(\mathbf{k})$ is the Fourier transform of δT_b . Hereafter $P_{x,x}$ is the auto-power spectrum of the field x , and $P_{x,y}$ is the cross-power spectrum of the fields x and y .

In Fig. 1 we present slices for three versions of the three-

dimensional power spectrum, the first being the one without including any effects of peculiar velocities (hereafter dubbed the “uncorrected for peculiar velocity”, or UPV, scheme), given by

$$P_{\Delta T}^{\text{UPV},3D}(\mathbf{k}) = \widehat{\delta T_b}^2(z_{\text{cos}}) P_{\delta r_{\rho_{\text{HI}}}, \delta r_{\rho_{\text{HI}}}}(\mathbf{k}). \quad (3)$$

The second version is calculated according to the “linear $\mu_{\mathbf{k}}$ -decomposition scheme” (Barkana & Loeb 2005; but see the exact definition and re-derivation in Section 5.3 below),

$$P_{\Delta T}^{s,\text{lin},3D}(\mathbf{k}) = \widehat{\delta T_b}^2(z_{\text{cos}}) \left[P_{\delta r_{\rho_{\text{HI}}}, \delta r_{\rho_{\text{HI}}}}(k) + 2 P_{\delta r_{\rho_{\text{HI}}}, \delta r_{\rho_{\text{HI}}}}(k) \mu_{\mathbf{k}}^2 + P_{\delta r_{\rho_{\text{HI}}}, \delta r_{\rho_{\text{HI}}}}(k) \mu_{\mathbf{k}}^4 \right]. \quad (4)$$

Here $\mu_{\mathbf{k}} \equiv k_{\parallel}/|\mathbf{k}|$ where k_{\parallel} is the LOS component of \mathbf{k} . Here the moments in the RHS of Eqn.(4) are angle-averaged in a spherical \mathbf{k} -space shell with $k = |\mathbf{k}|$, i.e., $P_{\delta_{\rho_{\text{HI}}}, \delta_{\rho_{\text{HI}}}}^{\delta_r}(k) = \langle P_{\delta_{\rho_{\text{HI}}}, \delta_{\rho_{\text{HI}}}}^{\delta_r}(\mathbf{k}) \rangle$, etc. Note that in Eqn. (4), the linear $\mu_{\mathbf{k}}$ -decomposition power spectrum can be computed directly from the real-space data, avoiding the need to specify a computational scheme for calculating the redshift-space-distorted 21cm signal data cube.

The third version of the three-dimensional power spectrum of 21cm brightness temperature fluctuations shown in Fig. 1 is calculated using a numerical scheme that finds the fully nonlinear redshift-space-distorted 21cm brightness temperature signal as a function of position and frequency (the ‘‘PPM-RRM’’ scheme, see Section 6.1.1). This last version of $P_{\Delta T}^{3\text{D}}(\mathbf{k})$ will be derived here in the sections which follow, based on the results of numerical reionization simulations.

The simulation data used for Fig. 1 are taken from a radiative transfer (RT) simulation of a $114 h^{-1}$ Mpc box with 256^3 RT resolution (more fully presented in Section 6.2). For the UPV scheme (top left), the power spectrum is seen to be numerically fluctuating in equal- $|\mathbf{k}|$ shells, but otherwise to be isotropic in the sense that it does not show any directional preference. For the linear $\mu_{\mathbf{k}}$ -decomposition scheme (top right), the power spectrum is perfectly distorted along the LOS direction, i.e. elongated for small k and squeezed for large k . For the PPM-RRM scheme (bottom center), it is hard to see the distortion for the small- k modes due to the small number of modes, but the compressed nature of the large- k modes is clearly visible, albeit with some numerical noise. Clearly, peculiar velocities introduce noticeable anisotropies in the 21cm power spectra.

To illustrate that the effects are not limited to Fourier space, we plot in Fig. 2 five samples of 21cm brightness temperature spectra along the LOS calculated with the ‘‘PPM-RRM’’ scheme (red curves), and the difference between these spectra and those calculated with the UPV scheme (blue curves). This shows that locally the difference between distorted and undistorted spectra can be comparable to the signal itself. Neglecting the peculiar velocity can thus result in significant errors when predicting the observational signal.

To make a more quantitative comparison, we compute the angle-averaged power spectrum $P_{\Delta T}^{s,\text{lin},1\text{D}}(k) = \langle P_{\Delta T}^{s,\text{lin},3\text{D}}(\mathbf{k}) \rangle$ for the linear $\mu_{\mathbf{k}}$ -decomposition scheme,

$$P_{\Delta T}^{s,\text{lin},1\text{D}}(k) = \widehat{\delta T}_b^2(z_{\text{cos}}) \left[P_{\delta_{\rho_{\text{HI}}}, \delta_{\rho_{\text{HI}}}}^{\delta_r}(k) + \frac{2}{3} P_{\delta_{\rho_{\text{HI}}}, \delta_{\rho_{\text{HI}}}}^{\delta_r}(k) + \frac{1}{5} P_{\delta_{\rho_{\text{HI}}}, \delta_{\rho_{\text{HI}}}}^{\delta_r}(k) \right], \quad (5)$$

as a function of $k = |\mathbf{k}|$, and the same for the UPV scheme, $P_{\Delta T}^{\text{UPV},1\text{D}}(k) = \widehat{\delta T}_b^2(z_{\text{cos}}) P_{\delta_{\rho_{\text{HI}}}, \delta_{\rho_{\text{HI}}}}^{\delta_r}(k)$. Fig. 3 shows the ratio of these two, $P_{\Delta T}^{s,\text{lin},1\text{D}}(k)/P_{\Delta T}^{\text{UPV},1\text{D}}(k)$, for ten different phases of reionization. Two limiting cases are obvious: for the early phases of reionization, the ratio approaches an almost constant value of 1.87; for the late phases the ratio tends to 1.0. These limits hold best at low k . They can be understood as follows. At early times, the neutral fraction fluctuations $\delta_{x_{\text{HI}}}^r$ are negligible, i.e. the neutral hydrogen density traces the total hydrogen density almost exactly, and, therefore, the 21cm power spectrum in the linear $\mu_{\mathbf{k}}$ -decomposition scheme differs from $P_{\Delta T}^{\text{UPV},1\text{D}} \approx \widehat{\delta T}_b^2(z_{\text{cos}}) P_{\delta_{\rho_{\text{HI}}}, \delta_{\rho_{\text{HI}}}}^{\delta_r}$ by a factor of $1 + \frac{2}{3} + \frac{1}{5} = 1.87$. At late times, neutral fraction fluctuations

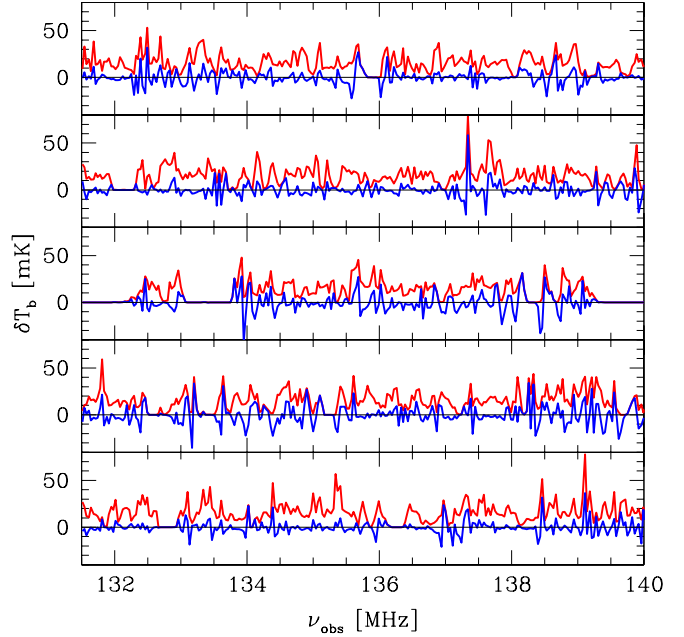


Figure 2. Sample LOS 21cm spectra from our numerical simulation at the 50% ionized epoch ($z = 9.457$). The figure shows the redshift-space-distorted brightness temperature (red) and the difference between the distorted and the undistorted (UPV) spectra (blue).

dominate over density fluctuations⁹, so its auto-power $P_{\delta_{x_{\text{HI}}}, \delta_{x_{\text{HI}}}}^{\delta_r}$ becomes the dominant term in both versions of the power spectra, making their ratio approach unity.

Between these two limits, Fig. 3 shows that as reionization proceeds the ratio evolves rather nonlinearly, changing both amplitude and shape non-monotonically. Reionization proceeds ‘‘inside-out’’ in our simulation, i.e. overdense regions ionize earlier than underdense regions, so the cross-power $P_{\delta_{\rho_{\text{HI}}}, \delta_{x_{\text{HI}}}}^{\delta_r}$ between density fluctuation and neutral fraction fluctuation is negative at large scales. Shortly after the onset of reionization ($x_i \lesssim 0.2$), the total density power spectrum $P_{\delta_{\rho_{\text{HI}}}, \delta_{\rho_{\text{HI}}}}^{\delta_r}$ still dominates over the other terms, but the cross-power $P_{\delta_{\rho_{\text{HI}}}, \delta_{x_{\text{HI}}}}^{\delta_r}$ also contributes significantly and is the next most important term, so $P_{\Delta T}^{s,\text{lin},1\text{D}}/P_{\Delta T}^{\text{UPV},1\text{D}} \approx (1.87 P_{\delta_{\rho_{\text{HI}}}, \delta_{\rho_{\text{HI}}}}^{\delta_r} + 2.67 P_{\delta_{\rho_{\text{HI}}}, \delta_{x_{\text{HI}}}}^{\delta_r}) / (P_{\delta_{\rho_{\text{HI}}}, \delta_{\rho_{\text{HI}}}}^{\delta_r} + 2 P_{\delta_{\rho_{\text{HI}}}, \delta_{x_{\text{HI}}}}^{\delta_r}) \approx 1.87 - 1.07 (P_{\delta_{\rho_{\text{HI}}}, \delta_{x_{\text{HI}}}}^{\delta_r} / P_{\delta_{\rho_{\text{HI}}}, \delta_{\rho_{\text{HI}}}}^{\delta_r})$, moving the ratio up since the neutral fraction fluctuations increase as reionization proceeds. When reionization reaches the midway point ($x_i \gtrsim 0.4$) and large ionized bubbles have formed, the neutral fraction auto-power $P_{\delta_{x_{\text{HI}}}, \delta_{x_{\text{HI}}}}^{\delta_r}$ starts dominating over other powers and the cross-power $P_{\delta_{\rho_{\text{HI}}}, \delta_{x_{\text{HI}}}}^{\delta_r}$ becomes subleading, so $P_{\Delta T}^{s,\text{lin},1\text{D}}/P_{\Delta T}^{\text{UPV},1\text{D}} \approx 1 + (2/3) (P_{\delta_{\rho_{\text{HI}}}, \delta_{x_{\text{HI}}}}^{\delta_r} / P_{\delta_{\rho_{\text{HI}}}, \delta_{\rho_{\text{HI}}}}^{\delta_r}) \approx 1 + (2/3) (P_{\delta_{\rho_{\text{HI}}}, \delta_{x_{\text{HI}}}}^{\delta_r} / P_{\delta_{x_{\text{HI}}}, \delta_{x_{\text{HI}}}}^{\delta_r})$. Since the cross power $P_{\delta_{\rho_{\text{HI}}}, \delta_{x_{\text{HI}}}}^{\delta_r}$ is negative, the ratio is less than unity. As reionization proceeds towards its final stages, the neutral fraction fluctuations continue to grow, pushing the ratio closer and closer to unity. Between

⁹ The variance in neutral fraction can be estimated as $(\Delta x_{\text{HI}})^2 = \langle (x_{\text{HI}} - \bar{x}_{\text{HI}})^2 \rangle \approx \bar{x}_{\text{HI}}(1 - \bar{x}_{\text{HI}})$, so the rms neutral fraction fluctuation is $\delta_{x_{\text{HI}}}^{\text{rms}} = \Delta x_{\text{HI}}/\bar{x}_{\text{HI}} \approx \sqrt{(1 - \bar{x}_{\text{HI}})/\bar{x}_{\text{HI}}}$. Thus the neutral fraction fluctuations grow as reionization proceeds, even though the variance in neutral fraction decreases near the end of reionization.

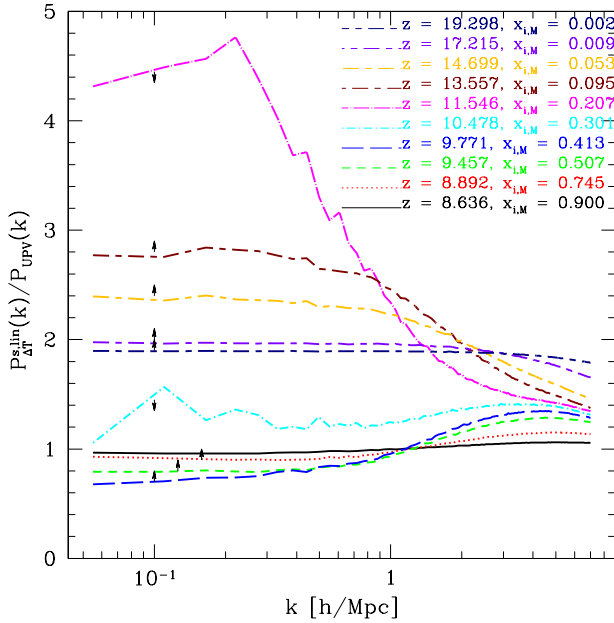


Figure 3. Ratio of 21cm redshift-space-distorted power spectrum in the linear μ_k -decomposition scheme and 21cm power spectrum in the UPV scheme as a function of comoving wavenumber k , at a series of redshift z and mass-averaged ionization fraction $x_{i,M}$. Arrows indicate the direction of the evolution of the curves at low k as reionization proceeds. Starting from the curve at $x_{i,M} = 0.002$ (dark blue, short dash - long dash) near the ratio = 1.87 limit, the ratio at low k moves up through the curves, in sequence, at $x_{i,M} = 0.009$ (purple, short dash - long dash), $x_{i,M} \approx 0.05$ (orange, short dash - long dash), $x_{i,M} \approx 0.1$ (dark red, short dash - long dash), flips the direction at $x_{i,M} \approx 0.2$ (magenta, dot - long dash), then moves down through the curves at $x_{i,M} \approx 0.3$ (cyan, dot - short dash), flips the direction again at $x_{i,M} \approx 0.4$ (blue, long dash), moves up through the curves at $x_{i,M} \approx 0.5$ (green, short dash), $x_{i,M} \approx 0.75$ (red, dot), and approaches the curve at $x_{i,M} \approx 0.9$ (black, solid) near the ratio = 1 limit.

$x_i \approx 0.2$ and 0.4 , the competition between neutral fraction fluctuations and density fluctuations makes the ratio at large scales first turn around at a large value $\sim 4 - 5$ ($x_i \approx 0.2$), then move all the way down to less than 1 ($x_i \approx 0.4$), then turn around again and begin to approach the limit of 1.

These comparisons illustrate the nontrivial effects when applying redshift space distortions using the linear μ_k -decomposition scheme. However, the fully nonlinearly distorted 21cm power spectrum may well show a more complicated behavior, which has not been previously explored. In order to calculate the fully-nonlinear redshift-space-distorted 21cm power spectrum, we need a robust scheme to compute it from simulation results. The aim of this paper is to develop such a scheme, taking into account all peculiar velocity effects. In a subsequent paper we will use this scheme to study the nonlinear distortion in the 21cm power spectrum and test the validity of linear μ_k -decomposition scheme upon which the 21cm cosmology is based.

3 TERMINOLOGY

Before we proceed to the main content, we summarize in this section our terminology which otherwise may be confusing.

3.1 Reference Frames

We distinguish between different reference frames. These are

- **Emitter space:** the local rest-frame of the emitting atoms.
- **FRW space:** the cosmic reference frame in which space is uniformly expanding, as described by the Friedmann-Robertson-Walker metric.

The emitter space and the FRW space are related by the local Lorentz transformation at the position of emitting atoms, and the relative motion of these two frames is the peculiar velocity of atoms.

From the observer’s point of view, the coordinates of source (t, \mathbf{r}) in FRW space can be relabeled by t_{arrival} (arrival time of radiation emitted at time t by source located at comoving location \mathbf{r}), z_{cos} (cosmological redshift experienced by photons from time t of their emission to the time t_{arrival} at which they reach the observer), and Θ (angular coordinates on the sky).

• **Observer real space:** for fixed $t_{\text{arrival}} = t_{\text{present}}$ (present time), the observer can reconstruct a part of the FRW space theoretically – those (t, \mathbf{r}) on the light-cone that can be determined by z_{cos} . In particular, $r = r(z_{\text{cos}})|_{t_{\text{present}}} = \int_0^{z_{\text{cos}}} c dz'/H(z')$. We call this the observer real space. In the rest of this paper, quantities measured in real space are superscripted with r , so for example n^r is a number density in real space.

• **Observer redshift space:** in practice, observers can only measure the observed redshift of radiation, since the wavelength is redshifted both cosmologically and by the Doppler shift associated with peculiar velocity, $\nu_{\text{obs}} = \nu_0/(1 + z_{\text{obs}})$ and $1 + z_{\text{obs}} = (1 + z_{\text{cos}})(1 - \frac{v_{\parallel}}{c})^{-1}$. Observers can set up a “distorted” comoving coordinate system, known as observer redshift space, in which the position of the emitter is the *apparent* comoving position if the redshift is interpreted as only cosmological, i.e. $s \equiv r(z_{\text{obs}})|_{t_{\text{present}}} = \int_0^{z_{\text{obs}}} c dz'/H(z')$, which shifts the *real* comoving coordinate r along the LOS (\hat{r}) to

$$\mathbf{s} = \mathbf{r} + \frac{(1 + z_{\text{obs}})}{H(z_{\text{obs}})} v_{\parallel}(t, \mathbf{r}) \hat{r}. \quad (6)$$

Note that the transformation between observer real and redshift spaces is not covariant (in a general relativistic sense) or even Galilean invariant, since it does not preserve spatial intervals at fixed time. In the rest of this paper, quantities measured in observer redshift space are superscripted with s , so for example, n^s is a number density in redshift space.

3.2 3D Mapping Distortion

One can distinguish between several types of distortions, namely

• **Apparent location distortion in redshift-space:** when the observed frequency of a spectral line from a distant source is used to locate the source along the LOS, the answer depends upon solving Eqn. (6), which requires a knowledge of the LOS peculiar velocity of the source at the time of emission. The term “redshift-space distortion” usually refers to the error one makes in locating the source by assuming the peculiar velocity to be zero.

• **Brightness temperature distortion in real-space:** Radiative transfer effects can result in a modification of the observed 21cm brightness temperature due to gradients in the velocity field, as shown in Section 5.1. This effect is independent of the adoption of either real- or redshift-space. In other words, even if an observer could construct a 3D mapping of 21cm brightness temperature in observer real space by knowing the peculiar velocities along the

LOS, gradients in the peculiar velocity field can still modify the magnitude of brightness temperature.

- **21cm redshift-space distortion:** This is the combination of the previous two distortions, namely the apparent location distortion in redshift-space and the brightness temperature distortion in real-space. The observed 21cm signal is modified by the presence of peculiar velocities according to this combination.

3.3 Power Spectra

Power spectra can be calculated in different dimensions in \mathbf{k} -space and with different methods for applying the effects of peculiar velocities. We use the following terminology:

- **3D power spectrum** $P_{3D}(\mathbf{k})$: The power spectrum in three-dimensional \mathbf{k} -space.

- **1D power spectrum** $P_{1D}(k)$: The power spectrum in one-dimensional $|\mathbf{k}|$ -space (or simply k -space), obtained by averaging the 3D power spectrum over modes in spherical shells in \mathbf{k} -space: $P_{1D}(k) \equiv \langle P_{3D}(\mathbf{k}) \rangle_{\text{shell}}$ with $k = |\mathbf{k}|$.

- **21cm power spectrum:** An abbreviation of “power spectrum of 21cm brightness temperature fluctuations”.

- **21cm redshift-space-distorted power spectrum:** The 21cm power spectrum in observer redshift space, i.e. taking the *21cm redshift-space distortion* into account.

- **21cm real-space power spectrum:** The 21cm power spectrum evaluated *with* velocity gradient corrections and yet in real space, i.e., only taking into account the *brightness temperature distortion in real-space*.

- **21cm UPV power spectrum:** The 21cm power spectrum evaluated *without* any velocity gradient corrections and in real space, i.e. taking into account neither the *brightness temperature distortion in real-space* nor the *apparent location distortion in redshift-space*; “UPV” stands for “uncorrected for peculiar velocity”.

- **21cm $\mu_{\mathbf{k}}$ -decomposition power spectrum:** an abbreviation of 21cm power spectrum calculated with the “linear $\mu_{\mathbf{k}}$ -decomposition scheme” (see Section 3.4).

3.4 Computational Schemes

Below we develop different schemes for applying the effects of peculiar velocities. We summarize these here.

- **Linear theory:** A scheme to compute 21cm power spectrum in redshift-space, where all fields, density, velocity and ionization fraction, are linearized; introduced by Barkana & Loeb (2005).

- **Linear $\mu_{\mathbf{k}}$ -decomposition scheme:** A scheme to compute 21cm power spectrum in redshift-space, assuming the density and velocity fields to be linear, but without constraints on the ionization fraction field; introduced in Section 5.3.1.

- **PPM-RRM scheme** (“Particle-to-Particle-to-Mesh Real-to-Redshift-Space-Mapping”): A *particle-based* numerical scheme to construct the 21cm data cube in observer redshift space, using the real- to redshift-space re-mapping of density, velocity and ionization fraction data. Introduced in Section 6.1.1.

- **MM-RRM scheme** (“Mesh-to-Mesh Real-to-Redshift-Space-Mapping”): Same as the PPM-RRM scheme, but *grid-based*; introduced in Section 6.1.2.

- **DEMRF scheme** (“Direct Evaluation by Multiple Real-space FFTs”): A scheme to compute the 21cm power spectrum in redshift-space by a direct integration technique; introduced in Section 6.4.3.

4 21CM REDSHIFT SPACE DISTORTION: OPTICALLY THIN AND HIGH T_s LIMIT

In this section we consider the simplest scenario, namely in the limit of small optical depth and high spin temperature $T_s \gg T_{\text{CMB}}$, and show that in this limit, peculiar velocities affect the 21cm brightness temperature in an analogous way to the redshift-space distortion in galaxy redshift surveys.

Recall that galaxy redshift surveys can distinguish individual galaxies. In other words, galaxies can be counted directly. Peculiar velocities move galaxies to their apparent locations, thereby affecting the number density of galaxies in redshift-space. For 21cm surveys, however, individual 21cm-line emitters — each neutral hydrogen atom — cannot be resolved and the H I number density can only be inferred from the observed brightness temperature of 21cm emission. This fundamental difference from galaxy redshift surveys implies that radiative transfer effects associated with peculiar velocities must be taken into account when calculating the redshift-space distortion of the 21cm background.

In the optically thin limit, the emission from each individual H I atom can be regarded as independently transferred along the LOS. In the high spin temperature ($T_s \gg T_{\text{CMB}}$) limit, the stimulated emission/absorption is negligible compared to the spontaneous emission. Therefore when both limits apply, each H I atom can be thought of as an independently shining 21cm-line source with the intrinsic luminosity $L_{\nu_0} = h\nu_0 A_{10}$, where $\nu_0 = 21 \text{ cm}/c = 1420.4057 \text{ MHz}$, and $A_{10} = 2.85 \times 10^{-15} \text{ s}^{-1}$ is the Einstein spontaneous emission coefficient of the 21cm transition. Then the emissivity at frequency ν_{RF} in the emitter space is

$$j_{\nu}^{\text{RF}} = \frac{1}{4\pi} L_{\nu_0} n_1^r \phi(\nu_{\text{RF}}), \quad (7)$$

where $n_1^r \approx (3/4)n_{\text{HI}}$ is the number density of H I atoms in the upper hyperfine state in real-space. The function $\phi(\nu_{\text{RF}})$ is the line profile and satisfies the normalization condition $\int_{-\infty}^{\infty} \phi(\nu) d\nu = 1$. The radiative transfer equation in FRW space then becomes

$$\frac{dI_{\nu}}{d\xi} = j_{\nu}, \quad (8)$$

where I_{ν} is the comoving specific intensity of a light ray. The ray path can be labeled by the *proper* distance along it, $d\xi = c dt$, where t is the physical time. Since the emissivity transforms as ν^2 (see, e.g., Mihalas 1978), $j_{\nu} = (1 - \frac{v_{\parallel}}{c})^2 j_{\nu}^{\text{RF}}$ in FRW space. The observed specific intensity then is

$$I_{\nu_{\text{obs}}} = \frac{1}{4\pi} L_{\nu_0} \int a^3 (1 - \frac{v_{\parallel}}{c})^2 n_1^r \phi(\nu_{\text{RF}}) d\xi. \quad (9)$$

In the idealized case of no thermal broadening, the line profile is a δ -function peaked at the transition frequency seen from the emitter space, i.e.,

$$\phi(\nu_{\text{RF}}) = \delta(\nu_{\text{RF}} - \nu_0). \quad (10)$$

Therefore, the integration picks up the integrand evaluated at the location of emission. Using an identity, whose derivation will be described in Section 5,

$$\left| \frac{d\nu_{\text{RF}}}{d\xi} \right| = \frac{1}{c} \nu_0 H(a) \left| 1 + \frac{1}{aH(a)} \frac{dv_{\parallel}}{dr_{\parallel}} \right|, \quad (11)$$

where r_{\parallel} is the comoving LOS distance, we find that the observed specific intensity is

$$I_{\nu_{\text{obs}}} = \frac{cL_{\nu_0} a \nu_{\text{obs}}^2}{4\pi \nu_0^3 H(a)} \frac{n_1^r}{\left| 1 + \frac{1}{aH(a)} \frac{dv_{\parallel}}{dr_{\parallel}} \right|}. \quad (12)$$

Now we consider the distortion of apparent location. It happens that the number density in redshift-space n_1^s satisfies

$$n_1^s = \frac{n_1^r}{\left| 1 + \frac{1}{aH(a)} \frac{dv_{\parallel}}{dr_{\parallel}} \right|}, \quad (13)$$

since the number of H I atoms are preserved between real- and redshift-space, and the volume element in redshift-space is distorted as $\delta V^s = \delta V^r \left| 1 + \frac{1}{aH(a)} \frac{dv_{\parallel}}{dr_{\parallel}} \right|$. Therefore we find that

$$I_{\nu_{\text{obs}}} = \frac{cL_{\nu_0} a \nu_{\text{obs}}^2}{4\pi \nu_0^3 H(a)} n_1^s. \quad (14)$$

(We will express Eqn. 14 in terms of the familiar brightness temperature in Section 5.) This is to say, the simple proportionality relation between the specific intensity (or, brightness temperature) and the neutral hydrogen density is preserved with and without peculiar velocities.

There is a simple explanation for Eqn. (14). In the limit of optically thin and high spin temperature, 21cm radiation from each neutral atom is emitted and then transferred independently. Therefore, the radiative transfer effects of peculiar velocity on a pocket of gas is simply equivalent to the simple picture of having all emitters shine from their apparent locations. Note that this net effect combines the peculiar velocity effects on the radiative transfer and on the distortion of apparent locations of sources.

Eqn. (14) establishes that, in this limit, there is an analogy between 21cm brightness temperature measurements and galaxy number density measurements, in that the neutral hydrogen atom number in 21cm tomography corresponds to the galaxy number in galaxy surveys. Therefore the 21cm power spectrum should be affected by peculiar velocities in a form similar to the linear redshift space distortion on large scales (first shown by Barkana & Loeb 2005), similar to the galaxy matter power spectrum (Kaiser 1987). In both cases, the effects of peculiar velocities can be thought of as the distortion due to displacing sources to their apparent LOS locations.

In the more general case in which optical depth is not small and/or $T_s \lesssim T_{\text{CMB}}$, however, the analogy between the redshift-space distortion of the 21cm background signal and that in galaxy redshift surveys breaks down. Since galaxy redshift surveys can resolve and count discrete galaxies, they do not depend upon measuring the unresolved intensity of galactic emission to deduce the number density of galaxies. For the 21cm background, however, we cannot resolve individual sources, (i.e. individual atoms), so we must use the specific intensity (or brightness temperature) to infer the source density, e.g. in the optically-thin/high T_s limit, according to Eqn. (14) above. If the conditions of low optical depth and high spin temperature are not satisfied, however, Eqn. (14) no longer applies. In that case, the luminosity emitted per atom then depends upon the unknown spin temperature, and the received intensity is also no longer linear in the optical depth. In order to interpret redshift-space-distorted 21cm maps, in general, therefore, we cannot simply borrow the analogy of the galaxy redshift surveys. We discuss the details of this in Section 5.

5 EFFECTS OF PECULIAR VELOCITY ON THE OBSERVED 21CM BACKGROUND

Given density, velocity, and ionization information in real space, peculiar velocities can affect the observed 21cm signal through two

effects: (1) the observed 21cm brightness temperature can be modified by the gradient of radial peculiar velocity of the gas along the LOS, and (2) the *apparent* location of the gas can be shifted from its *real*-space location because of the Doppler shift due to its peculiar velocity. We will address the first effect in Section 5.1, and then combine both effects to form a self-consistent picture of 21cm redshift space distortion in Sections 5.2 and 5.3.

5.1 The Transfer of 21cm Radiation Through the Intergalactic Medium

The effect of peculiar velocity gradients on *observed* 21cm brightness temperature was first addressed in Bharadwaj, Nath & Sethi (2001) and subsequently in Bharadwaj & Ali (2004), and Barkana & Loeb (2005). Bharadwaj, Nath & Sethi (2001) and Bharadwaj & Ali (2004) only explored the simpler limit of high spin temperature ($T_s \gg T_{\text{CMB}}$) and optically thin radiative transfer, and implicitly assumed that the velocity gradient is small so that the factor $1/\left(1 + \frac{1}{aH(a)} \frac{dv_{\parallel}}{dr_{\parallel}}\right)$ can be linearized. Barkana & Loeb (2005) attributed this velocity gradient correction to the effect of the fixed thermal width of the 21cm scattering cross section, without showing the details of the derivation. Since we aim to understand peculiar velocity thoroughly, it is worthwhile to re-derive this effect from first principle, i.e., solving the radiative transfer equation, and keeping all contributions of peculiar velocity to linear order v/c . In this section we show that it is the peculiar velocity of the *bulk motion*, not the *thermal* broadening, that is responsible for making its correction in 21cm brightness temperature. We check the validity of the optically thin approximation and show that it can break down in certain conditions, although it is mostly valid in the IGM. We find also that, in addition to the well-known velocity gradient correction, the contribution of spin temperature to 21cm brightness temperature can be modified by a term of order $\mathcal{O}(v/c)$.

5.1.1 The Formal Solution

Consider a light ray with *comoving* specific intensity I_{ν} ¹⁰ passing through a gas element. In an expanding universe, in which $\nu \propto 1/a$, the radiative transfer equation reads (Gnedin & Ostriker 1997; Wise & Abel 2010; Zhang, Hui & Haiman 2007)

$$\frac{\partial I_{\nu}}{c a \partial \eta} + \frac{\hat{n}}{a} \cdot \nabla I_{\nu} - \frac{H(a)}{c} \frac{\partial I_{\nu}}{\partial \ln \nu} = -\kappa_{\nu} I_{\nu} + j_{\nu}, \quad (15)$$

where I_{ν} is a function of conformal time η , comoving coordinates \mathbf{r} , frequency ν and direction \hat{n} . Here a is the cosmic scale factor and $H(a)$ is the Hubble constant at a . The ray path can be labeled by the *proper* distance along it, $d\xi = c dt$, where t is the physical time. The radiative transfer equation can be rewritten in terms of the Lagrangian total derivative

$$\frac{dI_{\nu}}{d\xi} = -\kappa_{\nu} I_{\nu} + j_{\nu}. \quad (16)$$

Here κ_{ν} and j_{ν} are the absorption coefficient and the *comoving* spontaneous emission coefficient at the frequency ν in FRW space, respectively.

We label ν_{obs} to be the frequency observed today, $\nu' = \nu_{\text{obs}}/a$ the frequency at some proper distance ξ' along the ray path

¹⁰ It is sometimes customary to use the *proper* specific intensity $I_{\nu}^{(p)}$, which is related to the comoving specific intensity by $I_{\nu} = I_{\nu}^{(p)} a^3$.

in FRW space, and $\nu_{\text{RF}} = \nu'(1 - \frac{v_{\parallel}}{c})^{-1}$ the frequency in emitter space, where v_{\parallel} is the radial proper peculiar velocity of the gas. Hereafter, the subscript or superscript ‘‘RF’’ stands for ‘‘rest-frame’’.

By defining the optical depth τ_{ν} forward along the ray path as

$$d\tau'_{\nu'} \equiv \kappa_{\nu'} d\xi', \quad (17)$$

the radiative transfer equation has the formal solution for the specific intensity observed today at frequency ν_{obs}

$$I_{\nu_{\text{obs}}} = I_{\nu_{\text{obs}}}^{\text{CMB}} e^{-\tau_{\nu_{\text{obs}}}} + \int_0^{\tau_{\nu_{\text{obs}}}} S_{\nu'}(\xi') e^{-(\tau_{\nu_{\text{obs}}} - \tau'_{\nu'})} d\tau'_{\nu'}. \quad (18)$$

Here we assume that the ray has the same comoving specific intensity as the CMB ($I_{\nu_{\text{obs}}}^{\text{CMB}}$) when the ray was on the far side of the gas element from the observer. $S_{\nu'}(\xi') = j_{\nu'}/\kappa_{\nu'}$ is the *comoving* source function at the frequency ν' seen in FRW space at the proper distance ξ' on the ray path. $\tau_{\nu_{\text{obs}}}$ is the integrated optical depth through the gas.

5.1.2 Optical Depth

In emitter space, the absorption coefficient is

$$\kappa_{\nu}^{\text{RF}} = \frac{1}{c} h\nu_0 (n_0 B_{01} - n_1 B_{10}) \phi(\nu_{\text{RF}}), \quad (19)$$

where B_{01} and B_{10} are the Einstein probability coefficients for induced upward and downward transitions, respectively, between the lower state with density n_0 and higher state with density n_1 . The spin temperature is defined to be the excitation temperature between the hyperfine states, i.e.

$$\frac{n_1}{n_0} \equiv \frac{g_1}{g_0} e^{-T_{\star}/T_s} = 3e^{-T_{\star}/T_s}, \quad (20)$$

where $g_0 = 1$ and $g_1 = 3$ are the statistical weights. $T_{\star} \equiv h\nu_0/k_B = 0.068$ K is the temperature corresponding to the rest-frame frequency ν_0 . For 21cm transitions, all astrophysical applications satisfy $T_s \gg T_{\star}$, so $n_0 = n_{\text{HI}}/4$ where n_{HI} is the *proper* number density of neutral hydrogen.¹¹ It is straightforward to show that

$$\kappa_{\nu}^{\text{RF}} = \frac{3c^2 A_{10} T_{\star} n_{\text{HI}} \phi(\nu_{\text{RF}})}{32\pi\nu_0^2 T_s}, \quad (21)$$

using the identities $g_1 B_{10} = g_0 B_{01} = c^3 g_1 A_{10}/8\pi h\nu_0^3$.

Now we transform our calculation to FRW space. The absorption coefficient transforms as ν^{-1} (see, e.g., Mihalas 1978), so in FRW space

$$\kappa_{\nu'} = \kappa_{\nu}^{\text{RF}} (\nu_{\text{RF}}/\nu') = \kappa_{\nu}^{\text{RF}} (1 - \frac{v_{\parallel}}{c})^{-1}. \quad (22)$$

Therefore the optical depth is

$$\tau_{\nu_{\text{obs}}} = \int \kappa_{\nu'} d\xi' = \int \frac{3c^2 A_{10} T_{\star} n_{\text{HI}}}{32\pi\nu_0^2 T_s (1 - \frac{v_{\parallel}}{c})} \phi(\nu_{\text{RF}}) d\xi'. \quad (23)$$

For the 21cm line transition, in the idealized case of no thermal broadening, the line profile is $\phi(\nu_{\text{RF}}) = \delta(\nu_{\text{RF}} - \nu_0)$. Integrating a δ -function picks up the integrand evaluated at the peak which physically corresponds to the location on the ray path where the transition actually takes place, its proper distance labeled as ξ_r

¹¹ Note that strictly speaking, n_{HI} is the number density in emitter space. But the number densities in emitter space and in FRW space only differ in the relativistic limit, i.e., $n^{\text{RF}}/n^{\text{cos}} = dV_{\text{cos}}/dV_{\text{RF}} = dt_{\text{RF}}/dt = 1/\sqrt{1 - v^2/c^2}$, so we can ignore the difference to linear order v/c .

(hereafter in this section, the *subscript* r stands for ‘‘radiation’’). We assume that each ray with a given observed frequency only experiences one 21cm transition event along the ray path. (We discuss the multi-transition case in Section 5.1.7.) The line profile can be rewritten as

$$\phi(\nu_{\text{RF}}) = \frac{\delta(\xi' - \xi_r)}{|d\nu_{\text{RF}}/d\xi'|_{\xi_r}}. \quad (24)$$

Here we assume the non-singular case, i.e., $(d\nu_{\text{RF}}/d\xi')_{\xi_r} \neq 0$. (We discuss the singular case in Section 5.1.5.) We use the relation $\nu_{\text{RF}} = \nu_{\text{obs}} a^{-1} (1 - \frac{v_{\parallel}}{c})^{-1}$ to take the derivative $d\nu_{\text{RF}}/d\xi'$, and then evaluate it at ξ_r where $\nu_{\text{RF}} = \nu_0$. It is straightforward to show that

$$\left(\frac{d\nu_{\text{RF}}}{d\xi'} \right)_{\xi_r} = \frac{\nu_0}{a_r c} \frac{\partial V_{\parallel}}{\partial r_{\parallel}}, \quad (25)$$

where $V_{\parallel} = a r_{\parallel} H(a) + v_{\parallel}$ is the proper velocity along the LOS and

$$\frac{\partial V_{\parallel}}{\partial r_{\parallel}} = aH(a) + \frac{dv_{\parallel}}{dr_{\parallel}}, \quad (26)$$

with r_{\parallel} the comoving LOS distance. Therefore the optical depth is

$$\tau_{\nu_{\text{obs}}} = \frac{3c^3 A_{10} T_{\star} a_r n_{\text{HI}}(\xi_r)}{32\pi\nu_0^3 T_s(\xi_r) |\partial V_{\parallel}/\partial r_{\parallel}|_{\xi_r} (1 - \frac{v_{\parallel}(\xi_r)}{c})}. \quad (27)$$

5.1.3 Observed Brightness Temperature

Now we simplify the formal solution of radiative transfer equation. Since $d\tau'_{\nu'} \propto \delta(\xi' - \xi_r) d\xi'$, the integral in Eqn.(18) takes non-zero contribution only from $\xi' = \xi_r$, therefore $\int_0^{\tau_{\nu_{\text{obs}}}} S_{\nu'}(\xi') e^{-(\tau_{\nu_{\text{obs}}} - \tau'_{\nu'})} d\tau'_{\nu'} = S_{\nu'}(\xi_r) \int_0^{\tau_{\nu_{\text{obs}}}} e^{-(\tau_{\nu_{\text{obs}}} - \tau'_{\nu'})} d\tau'_{\nu'} = S_{\nu'}(\xi_r) (1 - e^{-\tau_{\nu_{\text{obs}}}})$.

In emitter space, $S_{\nu_0}^{\text{RF}} = 2k_B \nu_0^2 T_s(\xi_r)/c^2$, i.e. the Planck function evaluated with the spin temperature T_s at ξ_r . The source function transforms as ν^3 (see, e.g., Mihalas 1978), so the *comoving* source function in FRW space is

$$S_{\nu'}(\xi_r) = a_r^3 \left(\frac{\nu'}{\nu_0} \right)^3 S_{\nu_0}^{\text{RF}} = \frac{2k_B \nu_{\text{obs}}^2 T_s(\xi_r) a_r (1 - \frac{v_{\parallel}}{c})}{c^2}, \quad (28)$$

where a_r^3 accounts for the comoving factor.

Suppose the ray has the frequency $\nu_p = \nu_{\text{obs}}/a_p$ with some scale factor $a_p < a_r$, (i.e., when it is on the far side of the gas element from the observer,) and is in equilibrium with the CMB of temperature $T_{\text{CMB},p} = T_{\text{CMB},0}/a_p$. In the absence of intervening atoms, the comoving specific intensity observed today would be $I_{\nu_{\text{obs}}}^{\text{CMB}} = a_p^3 2k_B \nu_p^2 T_{\text{CMB},p}/c^2 = 2k_B \nu_{\text{obs}}^2 T_{\text{CMB},0}/c^2$.

The 21cm brightness temperature at the observed frequency ν_{obs} is defined by

$$I_{\nu_{\text{obs}}} \equiv \frac{2k_B \nu_{\text{obs}}^2}{c^2} T_b(\nu_{\text{obs}}). \quad (29)$$

¹² The factor $e^{-(\tau_{\nu_{\text{obs}}} - \tau'_{\nu'})}$ is a step function at $\xi' = \xi_r$, so more rigorously, the integral yields $\int_0^{\tau_{\nu_{\text{obs}}}} S_{\nu'}(\xi') e^{-(\tau_{\nu_{\text{obs}}} - \tau'_{\nu'})} d\tau'_{\nu'} = S_{\nu'}(\xi_r) \tau_{\nu_{\text{obs}}} [1 - (1 - e^{-\tau_{\nu_{\text{obs}}})} \eta(0)]$. The unit step function $\eta(x)$ at $x = 0$ is undefined in general, but using an identity intrinsic in this problem $1 - e^{-\tau_{\nu_{\text{obs}}}} = \int_0^{\tau_{\nu_{\text{obs}}}} e^{-(\tau_{\nu_{\text{obs}}} - \tau'_{\nu'})} d\tau'_{\nu'} = \tau_{\nu_{\text{obs}}} [1 - (1 - e^{-\tau_{\nu_{\text{obs}}})} \eta(0)]$, we can regulate $\eta(0)$ and obtain the same result.

From Eqn.(18) it is straightforward to show that

$$T_b(\nu_{\text{obs}}) = T_{\text{CMB},0} e^{-\tau_{\nu_{\text{obs}}}} + T_s(\xi_r) a_r \left(1 - \frac{v_{\parallel}}{c}\right) (1 - e^{-\tau_{\nu_{\text{obs}}}}). \quad (30)$$

The 21cm line is generally optically thin to the IGM, i.e. $\tau_{\nu_{\text{obs}}} \ll 1$. (We discuss the validity of this approximation in Section 5.1.6.) In this limit, the differential brightness temperature is

$$\begin{aligned} \delta T_b(\nu_{\text{obs}}) &\equiv T_b(\nu_{\text{obs}}) - T_{\text{CMB},0} \\ &= a_r \tau_{\nu_{\text{obs}}} \left[T_s(\xi_r) \left(1 - \frac{v_{\parallel}}{c}\right) - T_{\text{CMB}}(a_r) \right], \end{aligned} \quad (31)$$

or

$$\begin{aligned} \delta T_b(\nu_{\text{obs}}) &= \frac{3c^3 A_{10} T_* \bar{n}_{\text{HI}}(\mathbf{r}) a_r}{32\pi \nu_0^3 H(a_r) \left| 1 + (aH)^{-1} \frac{dv_{\parallel}}{dr_{\parallel}}(\mathbf{r}) \right|} \\ &\times \left[1 - \frac{T_{\text{CMB}}(a_r)}{T_s^{\text{eff}}(\mathbf{r})} \right], \end{aligned} \quad (32)$$

where \mathbf{r} is the real-space location of 21cm transition corresponding to the proper distance ξ_r on the ray path. $T_{\text{CMB}}(a_r) = T_{\text{CMB},0}/a_r$ is the CMB temperature at the time of 21cm transition. Here we define the *effective* spin temperature

$$T_s^{\text{eff}}(\mathbf{r}) \equiv T_s(\mathbf{r}) \left[1 - \frac{v_{\parallel}(\mathbf{r})}{c} \right]. \quad (33)$$

Note that Eqn. (34) only infers that the spin temperature manifests itself to 21cm brightness temperature and optical depth in a manner modified by the peculiar velocity, but this effect does not modify the level population of hydrogen hyperfine states, nor the spin temperature. The level population can in fact be modified by peculiar velocity through an effect pointed out by Chuzhoy & Shapiro (2006). This is however a different effect from the one in Eqn. (34) which is based on a *given* spin temperature.

Eqn.(33) is in agreement with the well-known equation in Barkana & Loeb (2005) except for the appearance of effective spin temperature T_s^{eff} . However, this modification is actually not important for two reasons. First, it is of order $\mathcal{O}(v/c)$ and the bulk motion of gas is mostly non-relativistic. Second, many research papers focus on the epoch during reionization when $T_{\text{CMB}}/T_s \ll 1$, when the spin temperature has a negligible effect on the brightness temperature.

For convenience, we define the mean¹³ brightness temperature in the limit $T_s \gg T_{\text{CMB}}$ as

$$\begin{aligned} \widehat{\delta T}_b(z_{\text{cos}}) &\equiv \frac{3c^3 A_{10} T_* \bar{n}_{\text{HI}}(z_{\text{cos}})}{32\pi \nu_0^3 (1 + z_{\text{cos}}) H(z_{\text{cos}})} \\ &= 23.88 \left(\frac{\Omega_b h^2}{0.02} \right) \sqrt{\frac{0.15}{\Omega_M h^2} \frac{1 + z_{\text{cos}}}{10}} \bar{x}_{\text{HI,m}}(z_{\text{cos}}) \text{ mK}, \end{aligned} \quad (34)$$

where the cosmological redshift is defined by $1 + z_{\text{cos}} \equiv 1/a_r$, $\bar{n}_{\text{HI}}(z_{\text{cos}})$ is the mean neutral hydrogen number density at z_{cos} , $\bar{x}_{\text{HI,m}}(z_{\text{cos}})$ is the mean mass-weighted neutral fraction at z_{cos} . Then we can rewrite Eqn.(33) in terms of fluctuations,

$$\delta T_b(\nu_{\text{obs}}) = \widehat{\delta T}_b(z_{\text{cos}}) \frac{1 + \delta_{\rho_{\text{HI}}}(\mathbf{r})}{|1 + \delta_{\partial_r v}(\mathbf{r})|} \left[1 - \frac{T_{\text{CMB}}(a_r)}{T_s^{\text{eff}}(\mathbf{r})} \right], \quad (35)$$

where $\delta_{\rho_{\text{HI}}}(\mathbf{r}) = [n_{\text{HI}}(\mathbf{r}) - \bar{n}_{\text{HI}}(z_{\text{cos}})]/\bar{n}_{\text{HI}}(z_{\text{cos}})$ is the neutral hydrogen density fluctuation, and $\delta_{\partial_r v}(\mathbf{r})$ is defined in Eqn. (2).

¹³ This is not a volume-weighted mean, but essentially a mean in the redshift-space. See footnote 23.

5.1.4 Line Profile Revisited: Velocity vs. Thermal Broadening

In general, the line profile can include thermal broadening, as well as velocity broadening due to bulk motion. The velocity broadening is naturally included by taking the δ -function-shaped line profile peaked at the rest-frame frequency which is shifted both cosmologically and by Doppler effect. Our calculation (Eqns. 27 and 36) shows that the velocity gradient correction is due to the bulk motion of neutral atoms. However, in their original paper, Barkana & Loeb (2005) explained the inclusion of the velocity gradient compactly, without showing details, as ‘‘The velocity gradient term arises because the 21 cm scattering cross section has a fixed thermal width, which translates through the redshift factor $(1 + v_r/c)$ to a fixed interval in velocity’’. This seems to mean that the thermal broadening is responsible for the velocity gradient correction. In this subsection, we will clarify that in the non-singular case, the contribution of thermal broadening is always subdominant to the velocity broadening.

Basically, the thermal velocity of hydrogen atoms can contribute an additional Doppler shift of the line frequency. For a given ν_{obs} , neutral atoms can in principle have a possibility, given by the Maxwellian distribution, of seeing the radiation in the 21cm rest-frame frequency ν_0 , even if ν_{RF} (with Doppler shifted due to bulk motion) $\neq \nu_0$. This is described by the Gaussian line profile, replacing Eqn. (10),

$$\phi(\nu_{\text{RF}}) = \frac{1}{\Delta \nu_{\text{th}} \sqrt{\pi}} \exp \left[-\frac{(\nu_{\text{RF}} - \nu_0)^2}{\Delta \nu_{\text{th}}^2} \right], \quad (36)$$

where

$$\Delta \nu_{\text{th}} = \frac{\nu_0}{c} \sqrt{\frac{2k_B T_k}{m_H}}, \quad (37)$$

is the thermal Doppler shift corresponding to a gas kinetic temperature T_k .

In the non-singular case, i.e. $(d\nu_{\text{RF}}/d\xi')_{\xi_r} \neq 0$, we can change the integration variable in Eqn. (23),

$$d\xi' = \frac{d\nu_{\text{RF}}}{|d\nu_{\text{RF}}/d\xi'|}, \quad (38)$$

and rewrite the optical depth with thermal broadening as

$$\tau_{\nu_{\text{obs}}}^{\text{T}} = \int_{-\infty}^{\infty} \tau_{\nu_{\text{obs}}}^{\text{NT}}(\xi') \phi(\nu_{\text{RF}}) d\nu_{\text{RF}}. \quad (39)$$

where $\tau_{\nu_{\text{obs}}}^{\text{NT}}(\xi')$ is the optical depth without thermal broadening, i.e. Eqn. (27) with ξ_r replaced by ξ' corresponding to ν_{RF} .

Suppose the rest-frame frequency finds $\nu_{\text{RF}} = \nu_0$ at $\xi' = \xi_r$. The thermal width is small compared to ν_0 , since $\Delta \nu_{\text{th}}/\nu_0 \sim 10^{-5}$ if $T_k \sim 10^4$ K. Therefore the integrand is nonzero only near $\nu_{\text{RF}} = \nu_0$. So we can Taylor expand the integrand at ν_0 to sub-leading order in $\mathcal{O}(\nu_{\text{RF}} - \nu_0)^2$, since the first order $\propto \int_{-\infty}^{\infty} d\nu_{\text{RF}} (\nu_{\text{RF}} - \nu_0) \exp \left[-\frac{(\nu_{\text{RF}} - \nu_0)^2}{\Delta \nu_{\text{th}}^2} \right] = 0$. It is straightforward to show that the result is

$$\tau_{\nu_{\text{obs}}}^{\text{T}} = \tau_{\nu_{\text{obs}}}^{\text{NT}}(\xi_r) \left[1 + \Delta \tau_{\nu_{\text{obs}}}^{\text{T}} \right], \quad (40)$$

where the fractional correction due to thermal broadening is

$$\Delta \tau_{\nu_{\text{obs}}}^{\text{T}} = \frac{1}{4\tau_{\nu_{\text{obs}}}^{\text{NT}}} \frac{d^2 \tau_{\nu_{\text{obs}}}^{\text{NT}}}{d\nu_{\text{RF}}^2} \Big|_{\nu_0} \Delta \nu_{\text{th}}^2 \sim \mathcal{O} \left(\frac{\Delta \nu_{\text{th}}}{\nu_0} \right)^2 \sim 10^{-9}. \quad (41)$$

Here we assume the gas temperature is about 10^4 K, which is close to the maximum temperature attainable by neutral hydrogen before

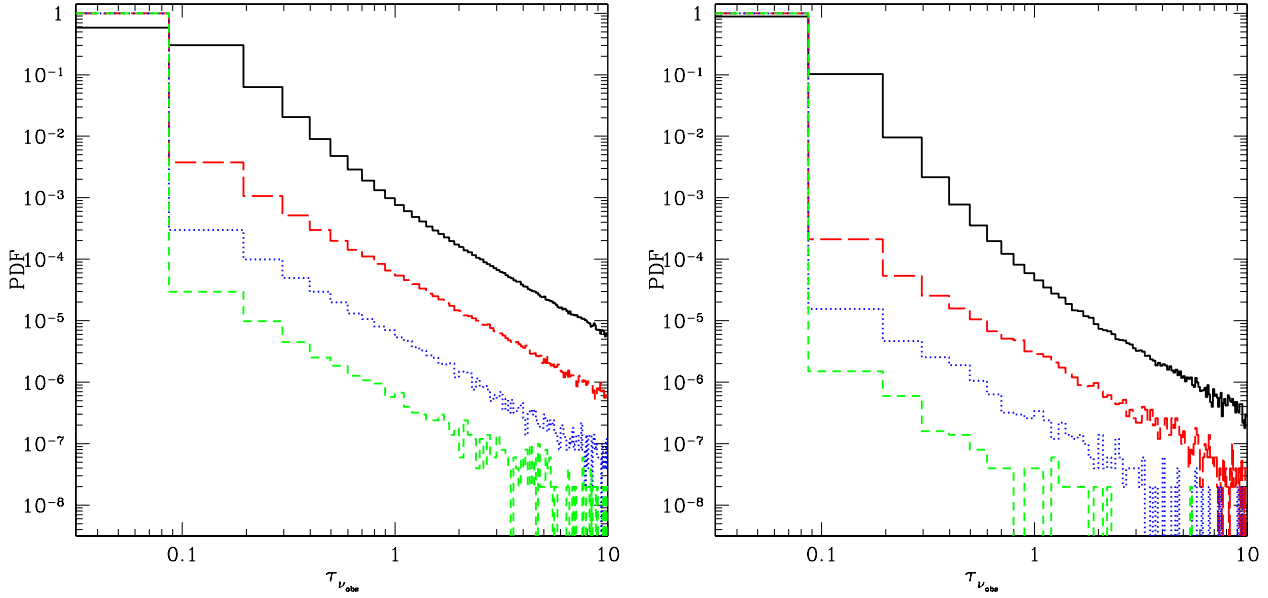


Figure 4. PDF of 21cm optical depth $\tau_{\nu_{\text{obs}}}$ from our simulation data at $z = 9.457$ (50% ionized). The simulation is in a 114 Mpc/h box with IGM particle data smoothed onto a 256^3 grid. PDF shows the probability of finding $\tau_{\nu_{\text{obs}}}$ in intervals of $\Delta\tau_{\nu_{\text{obs}}} = 0.1$. We assume $T_s/T_{\text{CMB}} = 0.1$ (solid, black), 1 (long-dashed, red), 10 (dotted, blue), and 100 (short-dashed, green). Left panel: assuming a fully neutral Universe ($x_{\text{HI}} = 1$). Right panel: using the actual ionization pattern from the simulation.

collisional ionization becomes important. Therefore, the contribution of thermal broadening is always negligible compared to the bulk motion.

5.1.5 Observed Brightness Temperature: Optically Thick Limit

Our results for optical depth and brightness temperature seem to diverge for $\delta_{\partial_r v} = -1$ (see Eqns. 27 and 36). We discuss this singularity behavior in this subsection, and find that the divergence in optical depth can be relaxed by including thermal broadening, and the divergence in brightness temperature can be removed by dropping the optically thin approximation.

We should first note that the singularity at $\delta_{\partial_r v} = -1$ corresponds to $(d\nu_{\text{RF}}/d\xi')_{\xi_r} = 0$. In this case, the regular changing variable technique (Eqn. 39) is invalid. Instead, one should Taylor expand $\nu_{\text{RF}}(\xi')$ near ξ_r to second order, $\nu_{\text{RF}} = \nu_0 + \frac{1}{2}\beta(\xi' - \xi_r)^2$, where $\beta = \left. \frac{d^2\nu_{\text{RF}}}{d\xi'^2} \right|_{\xi_r}$, and find that

$$d\xi' = \text{sgn}(\xi' - \xi_r) \text{sgn}(\beta) \frac{d\nu_{\text{RF}}}{\sqrt{2\beta(\nu_{\text{RF}} - \nu_0)}}. \quad (43)$$

Then the optical depth becomes

$$\begin{aligned} \tau_{\nu_{\text{obs}}} &= 2 \int_{\nu_0}^{\text{sgn}(\beta)\cdot\infty} d\nu_{\text{RF}} \text{sgn}(\beta) \frac{3c^2 A_{10} T_* n_{\text{HI}}}{32\pi\nu_0^2 T_s (1 - \frac{v_{\parallel}}{c})} \\ &\times \frac{\phi(\nu_{\text{RF}})}{\sqrt{2\beta(\nu_{\text{RF}} - \nu_0)}}. \end{aligned} \quad (44)$$

If there is no thermal broadening, the line profile is a δ -function peaked at $\nu_{\text{RF}} = \nu_0$, and the optical depth is still divergent due to the $1/\sqrt{\nu_{\text{RF}} - \nu_0}$ factor. However, thermal broadening can remove this divergence. To see this, we can move the ξ' -dependent factors (n_{HI} , T_s , and v_{\parallel}) out of the integral, evaluated at ξ_r , since

the evaluation is concentrated near ξ_r . When applying the thermal line profile (Eqn. 37), we find that the optical depth in the singular case ($\delta_{\partial_r v} = -1$) becomes

$$\tau_{\nu_{\text{obs}}} = \frac{3c^2 A_{10} T_* n_{\text{HI}}(\xi_r)}{32\pi\nu_0^2 T_s(\xi_r) (1 - \frac{v_{\parallel}(\xi_r)}{c})} \times \frac{1.446}{\sqrt{|\beta|\Delta\nu_{\text{th}}}}. \quad (45)$$

Here the factor 1.446 is an approximation of $\sqrt{2/\pi} \times 2\Gamma(5/4)$. Since $\tau_{\nu_{\text{obs}}} \propto 1/\sqrt{\Delta\nu_{\text{th}}}$, the optical depth can be large when $\delta_{\partial_r v}$ is close to -1 . We evaluate β when $\delta_{\partial_r v} = -1$,

$$\beta = -\frac{\nu_0 H(a_r)^2}{c^2} \left[2 + \frac{a_r H'(a_r)}{H(a_r)} - \frac{c}{(a_r H(a_r))^2} \frac{d^2 v_{\parallel}}{dr_{\parallel}^2} \Big|_{\xi_r} \right], \quad (46)$$

where $H'(a) = dH/da$.

There are two astrophysical cases that can generate $\delta_{\partial_r v} = -1$. One is the virialized halo and the other is the spherical collapse at the turn-around point (pre-virialization). In both cases, the proper velocity is $V_{\parallel} = a r_{\parallel} H(a) + v_{\parallel} = 0$ (seen from the halo center), so $dv_{\parallel}/dr_{\parallel} = -aH(a)$. Near the singular point, the optical depth can become large, thus invalidating the optically thin approximation. As a result, one cannot apply the popular equation (Eqn. 33) to evaluate the brightness temperature, but should instead use the exact solution

$$\delta T_b(\nu_{\text{obs}}) = a_r \left[T_s(\xi_r) \left(1 - \frac{v_{\parallel}}{c}\right) - T_{\text{CMB}}(a_r) \right] \left[1 - e^{-\tau_{\nu_{\text{obs}}}} \right] \quad (47)$$

where $\tau_{\nu_{\text{obs}}}$ is given by Eqn. (45) when $\tau_{\nu_{\text{obs}}} \gtrsim 1$ or Eqn. (27) when $\tau_{\nu_{\text{obs}}} < 1$ but not too small. The exact value of $\tau_{\nu_{\text{obs}}}$ is not important as long as $\tau_{\nu_{\text{obs}}} \gg 1$, since the τ -dependent term should saturate $1 - \exp(-\tau_{\nu_{\text{obs}}}) \approx 1$ for large $\tau_{\nu_{\text{obs}}}$, in which case the brightness temperature is still finite, i.e.

$$\delta T_b(\nu_{\text{obs}}) \approx a_r \left[T_s(\xi_r) \left(1 - \frac{v_{\parallel}}{c}\right) - T_{\text{CMB}}(a_r) \right] \quad (48)$$

instead of infinite as it would be using the popular Eqn. (33).

5.1.6 How Good is the Optically Thin Approximation during the EOR?

It is often assumed that 21cm line is optically thin, fundamentally because 21cm hyperfine transition is highly forbidden with an extremely small probability of $A_{10} = 2.85 \times 10^{-15} \text{ s}^{-1}$. However, peculiar velocity gradients can enhance the optical depth in overdense regions¹⁴. To see this, we rewrite the optical depth in Eqn. (27) as

$$\begin{aligned} \tau_{\nu_{\text{obs}}} &= \frac{\widehat{\delta T}_b(z_{\text{cos}})}{T_{\text{CMB},0}} \frac{1 + \delta_{\rho_{\text{HI}}}}{\alpha |1 + \delta_{\partial_r v}| (1 - \frac{v_{\parallel}}{c})} \\ &= 0.005 \left(\frac{\Omega_b h^2}{0.02} \right) \sqrt{\frac{0.15}{\Omega_M h^2} \frac{1 + z_{\text{cos}}}{10}} \frac{\bar{x}_{\text{HI},m}(z_{\text{cos}})}{0.5} \\ &\quad \times \frac{1 + \delta_{\rho_{\text{HI}}}}{\alpha |1 + \delta_{\partial_r v}| (1 - \frac{v_{\parallel}}{c})}, \end{aligned} \quad (49)$$

where $\alpha \equiv T_s(\mathbf{r})/T_{\text{CMB}}(z_{\text{cos}})$. For example in our reionization simulation at $z \sim 9$ when $\bar{x}_{\text{HI},m} \sim 0.5$, and with reasonable assumptions such as non-relativistic bulk motion $v \ll c$ and small fluctuation $1 + \delta_{\rho_{\text{HI}}} \sim 1$, the optical depth can become of order unity when the velocity gradient is very negative, such that $|1 + \delta_{\partial_r v}| \lesssim \frac{0.005}{\alpha}$, as can happen in some overdense regions. This condition on the velocity gradient widens when 21cm occurs in absorption ($T_s < T_{\text{CMB}}$) and becomes narrower when it occurs in emission ($T_s > T_{\text{CMB}}$).

Fig. 4 shows the PDF of the $\tau_{\nu_{\text{obs}}}$ distribution of the IGM from our simulation data (see simulation details in Section 6.2). We smooth the N-body particle mass in the IGM onto a regular 256^3 grid, compute the cell's velocity gradient using the SPH-like smoothing method described in Appendix A, and compute the optical depth of the IGM. For simplicity, we drop the $1 - v/c$ factor in the optical depth calculation by assuming non-relativistic bulk motions. Fig. 4(a) shows the extent by which velocity gradients alone can enhance the optical depth, by assuming $\delta_{\rho_{\text{HI}}} = \delta_{\rho_{\text{H}}}$. The PDF at large optical depth increases by roughly an order of magnitude when we decrease the spin temperature by an order of magnitude. In the pessimistic case ($T_s/T_{\text{CMB}} = 0.1$), as many as 0.1% of the total cells have an optical depth of order unity.

In Fig. 4(b), we plot the same PDF for the actual $\delta_{\rho_{\text{HI}}}$ from the reionization simulation. Due to the ‘‘inside-out’’ character of reionization, the overdense regions that can have velocity gradients close to -1 ionize first and one can expect the effect to be much less. Fig. 4(b) shows that for the case $T_s/T_{\text{CMB}} = 0.1$, only a fraction of up to 10^{-4} of the total number cells approach an optical depth of 1. For the case $T_s/T_{\text{CMB}} = 100$ this fraction becomes as low as 10^{-7} . We therefore conclude that we can safely use the optically thin approximation when calculating the 21cm radiation from the IGM.

However, we should note that the optically thin approximation may break down to a larger extent in one of the two following scenarios.

(i) 21cm radiation from a halo or in spherical collapse at the turn-around point may be mostly optically thick, because $\delta_{\partial_r v} \sim -1$ there. The breakdown of the optically thin approximation may be more prominent when the 21cm line is in absorption against the CMB.

¹⁴ Iliev et al. (2002) showed that the 21cm line can become optically thick inside dense mini-halos, but this is a different effect from the enhancement due to velocity gradients we consider here.

(ii) When the 21cm radiation is computed directly from high-resolution particle data (and not from gridded data as above), a larger fraction of particles can be optically thick, since the particle density is higher in overdense regions.

The breakdown of the optically thin approximation merits more investigation beyond the scope of this paper where we focus on 21cm radiation from the IGM and this approximation is mostly valid. We defer further analysis to future work.

5.1.7 When the Mapping from Frequency to Position Along LOS is Multi-valued

In the case of multiple 21cm transitions along the ray path, we label the transition events by $i = 1, \dots, N$ in sequence along the forward ray path. The optical depth starts from $\tau_0 \equiv 0$ (on the far side of the gas element), to τ_i (after the ray passes through event i), and to $\tau_N = \tau_{\nu_{\text{obs}}}$. We define the differential optical depth $\Delta\tau_i \equiv \tau_i - \tau_{i-1} = \int_{\text{across } i} \kappa_{\nu'} d\xi'$ which can be evaluated using Eqn.(27) with the transition location $\xi_r \rightarrow \xi_i$. To carry out the integration in Eqn.(18), we split the integral into a sum of N sub-integrals each over only one transition event, i.e., $\int_0^{\tau_{\nu_{\text{obs}}}} \dots d\tau'_{\nu'} = \sum_{i=1}^N \int_{\tau_{i-1}}^{\tau_i} \dots d\tau'_{\nu'}$. Using the same trick as in Section 5.1.3, we find $\int_0^{\tau_{\nu_{\text{obs}}}} S_{\nu'}(\xi') e^{-(\tau_{\nu_{\text{obs}}} - \tau'_{\nu'})} d\tau'_{\nu'} = \sum_{i=1}^N S_{\nu'}(\xi_i) \Delta\tau_i$ in the *optically thin* limit. Using the fact that $\tau_{\nu_{\text{obs}}} = \sum_{i=1}^N \Delta\tau_i$, we find that $\delta T_b(\nu_{\text{obs}}) = \sum_{i=1}^N \delta T_b(\nu_{\text{obs}})|_{\xi_i}$, i.e. the observed differential brightness temperature is the sum of contributions from all transitions, where each contribution can be evaluated using the equation for a single transition (Eqn.33) with \mathbf{r} the position of each transition.

5.2 The Distortion of Apparent Location and Brightness Temperature by Peculiar Velocity

In Section 5.1 we derived the equation for the observed 21cm brightness temperature, evaluating physical properties at the *actual* location \mathbf{r} of the emitting neutral hydrogen atoms. However, observers can only determine the position of the source from the *observed* 21cm line frequency, i.e. in observer redshift space. To make theoretical predictions, it is therefore necessary to express the observed 21cm brightness temperature in observer redshift-space coordinates. This subsection deals with solving this issue.

5.2.1 Distinguishing the Two Distortion Effects by Peculiar Velocity

We should emphasize first that, although the effects of peculiar velocity on observed 21cm brightness temperature and on apparent location of sources are both due to the Doppler shift of the line frequency, the underlying mechanisms do differ. For the former, peculiar velocity distinguishes the emitter space from the FRW space, both of which are physical reference frames, and translates the difference between these two frames, through the transformation of the line profile, to the optical depth that affects the brightness temperature measured by observers today in FRW space. It is a ‘‘real’’ effect in the sense that peculiar velocities change the observed brightness temperature, regardless of how observers interpret the location of source.

For the latter, the observer redshift-space coordinates are simply an artificial coordinate system that could be replaced by the

observer real-space coordinates if observers could measure the peculiar velocities of sources and reconstruct the brightness temperature map in the sources' actual location. This is "artificial" in the sense that it is due to the observers' incomplete information on the location of the sources.

The observed brightness temperature we derived in Eqn. (36) is evaluated in terms of quantities measured in real space. We can rewrite Eqn. (36) as

$$\delta T_b^r(\mathbf{r}) = \widehat{\delta T}_b(z_{\text{cos}}) \frac{1 + \delta_{\rho_{\text{HI}}}^r(\mathbf{r})}{|1 + \delta_{\delta_{r,v}}^r(\mathbf{r})|} \left[1 - \frac{T_{\text{CMB}}(a_r)}{T_s^{r,\text{eff}}(\mathbf{r})} \right], \quad (50)$$

using the superscript "r" for real space explicitly. (See our convention of superscripts "r" and "s" in Section 3.1.) By definition, the brightness temperature calculated from redshift-space quantities, $\delta T_b^s(\mathbf{s})$, is equal to $\delta T_b^r(\mathbf{r})$. So in principle, we can combine the two effects of peculiar velocity and find an expression for the brightness temperature using redshift-space quantities from

$$\delta T_b^s(\mathbf{s}) = \delta T_b^r(\mathbf{r}(\mathbf{s})), \quad (51)$$

where $\mathbf{r}(\mathbf{s})$ is the inverse of the real-to-redshift-space mapping $\mathbf{r} \rightarrow \mathbf{s} = \mathbf{r} + \frac{(1+z_{\text{obs}})}{H(z_{\text{obs}})} v_{\parallel}(\mathbf{r}) \hat{r}$. We show below that this relation can be simplified for the 21cm brightness temperature. We restrict the discussion to calculating the 21cm brightness temperature in the optically thin approximation here, since this is mostly valid in the IGM.

5.2.2 21cm Brightness Temperature in Observer Redshift Space: Mathematical Approach

We present the derivation of the equation for the 21cm brightness temperature in terms of redshift-space quantities in two ways. First in this subsection in a mathematical way, and in the next subsection in a more heuristic physical way. To simplify matters, we for now assume that $T_s \gg T_{\text{CMB}}$ and generalize our result to an arbitrary T_s in Section 5.2.4.

Analogous to redshift space distortion in galaxy surveys, where the number of galaxies is preserved between real- to redshift-space, the number of *emitting neutral hydrogen atoms* is preserved in the 21cm signal, i.e. $n_{\text{HI}}^s(\mathbf{s}) \delta V^s(\mathbf{s}) (1 + z_{\text{cos}})^{-3} = n_{\text{HI}}^r(\mathbf{r}) \delta V^r(\mathbf{r}) (1 + z_{\text{cos}})^{-3}$. From the real-to-redshift-space mapping, $\mathbf{s} = \mathbf{r} + \frac{(1+z_{\text{obs}})}{H(z_{\text{obs}})} v_{\parallel}(\mathbf{r}) \hat{r}$, it is easy to find the relation between comoving volume elements in both frames $\delta V^s(\mathbf{s}) = \delta V^r(\mathbf{r}) |1 + \delta_{\delta_{r,v}}^r(\mathbf{r})|$. Therefore, the number density measured in redshift space is

$$n_{\text{HI}}^s(\mathbf{s}) = \frac{n_{\text{HI}}^r(\mathbf{r})}{|1 + \delta_{\delta_{r,v}}^r(\mathbf{r})|}. \quad (52)$$

The mean number density must be preserved too, when averaged over a volume large enough to contain all gas of interest. In terms of fluctuations $\delta_{\rho_{\text{HI}}}^s(\mathbf{s}) = \frac{n_{\text{HI}}^s(\mathbf{s}) - \bar{n}_{\text{HI}}(z_{\text{cos}})}{\bar{n}_{\text{HI}}(z_{\text{cos}})}$, where \bar{n}_{HI} is the mean (physical) HI number density, we have $1 + \delta_{\rho_{\text{HI}}}^s(\mathbf{s}) = \frac{1 + \delta_{\rho_{\text{HI}}}^r(\mathbf{r})}{|1 + \delta_{\delta_{r,v}}^r(\mathbf{r})|}$, and hence in the $T_s \gg T_{\text{CMB}}$ limit,

$$\delta T_b^s(\mathbf{s}) = \frac{\widehat{\delta T}_b(z_{\text{cos}})}{\bar{n}_{\text{HI}}(z_{\text{cos}})} n_{\text{HI}}^s(\mathbf{s}) = \widehat{\delta T}_b(z_{\text{cos}}) [1 + \delta_{\rho_{\text{HI}}}^s(\mathbf{s})]. \quad (53)$$

This means that in the high T_s limit, the observed 21cm brightness temperature is directly proportional to the number density of neutral hydrogen atoms measured in observer redshift space. In other words, 21cm tomography maps exactly the neutral hydrogen distribution in redshift-space. This is the result we already found in Section 4, but now more rigorously derived.

In case of multiple transitions along the ray path, the brightness temperature is the sum of contributions from all transition events, as discussed in Section 5.1.7. Since these transitions correspond to the same observed frequency and therefore the same redshift-space location, Eqn.(53) still holds for the multi-transition case, since by definition the HI density in redshift-space is the linear addition of HI mass from all such transition spots per unit redshift-space volume.

5.2.3 21cm Brightness Temperature in Observer Redshift Space: Physical Approach

Now we rederive Eqn. (53) by considering the physical meaning of brightness temperature. The 21cm brightness temperature is simply proportional to the specific intensity, i.e. $\delta T_b(\nu_{\text{obs}}) = \frac{c^2}{2k_B \nu_{\text{obs}}^2} \delta I_{\nu_{\text{obs}}}$ where δI_{ν} is the differential specific intensity relative to CMB, and equal to the energy received from distant gas per unit observation time per unit transverse collection area per solid angle spanned by sources per unit observed frequency interval. The solid angle is proportional to the transverse area of the source, the observed frequency interval is proportional to the LOS distance interval in *redshift* space, and hence the energy received from a patch of sky near ν_{obs} per unit time per unit collection area is proportional to the brightness temperature times the *redshift*-space volume element. I.e., $d^2\Omega = dA_{\perp}^s/d_A^2(z_{\text{obs}})$, $d\nu_{\text{obs}} = |ds_{\parallel}|/y(z_{\text{obs}})$, and $dE/dt dA_{\text{coll}} = C(z_{\text{obs}}) \delta T_b(\nu_{\text{obs}}) \delta V^s$, where $d_A(z_{\text{obs}})$ is the comoving angular diameter distance¹⁵, $y(z_{\text{obs}}) = \lambda_0(1 + z_{\text{obs}})^2/H(z_{\text{obs}})$, dA_{\perp}^s is the comoving transverse area in redshift space, ds_{\parallel} is the comoving radial interval in redshift space, $C(z_{\text{obs}}) \equiv 2k_B \nu_{\text{obs}}^2/c^2 d_A^2(z_{\text{obs}}) y(z_{\text{obs}})$, and $\delta V^s = dA_{\perp}^s |ds_{\parallel}|$ is the comoving redshift-space volume element.

Consider a small region (e.g., a cell or a pixel) of the sky at the telescope's resolution scale. The detector simply smears subcell brightness temperature information by summing energies received from all unresolved subcells. For each subcell, $\delta T_b \delta V^s = \frac{\widehat{\delta T}_b(z_{\text{cos}})}{\bar{n}_{\text{HI}}(z_{\text{cos}})} \frac{n_{\text{HI}}(\mathbf{r})}{|1 + \delta_{\delta_{r,v}}^r(\mathbf{r})|} \times \delta V^r(\mathbf{r}) |1 + \delta_{\delta_{r,v}}^r(\mathbf{r})| = (1 + z_{\text{cos}})^3 \frac{\widehat{\delta T}_b(z_{\text{cos}})}{\bar{n}_{\text{HI}}(z_{\text{cos}})} \delta N_{\text{HI}}$, where $\delta N_{\text{HI}}(\mathbf{r}) = (1 + z_{\text{cos}})^{-3} n_{\text{HI}}(\mathbf{r}) \delta V^r(\mathbf{r})$ is the number of emitting neutral hydrogen atoms from the subcell at \mathbf{r} . Ignoring the difference of observed frequency and redshift between the subcells, the brightness temperature of the cell is $\delta T_b(\nu_{\text{obs}}) = \frac{1}{C(z_{\text{obs}}) \Delta V^s} \sum \left[\frac{dE}{dt dA_{\text{coll}}} \right]_{\text{sub}} = \frac{1}{\Delta V^s} \sum [\delta T_b \delta V^s]_{\text{sub}} = \widehat{\delta T}_b(z_{\text{cos}}) \frac{n_{\text{HI,cell}}^s}{\bar{n}_{\text{HI}}} = \widehat{\delta T}_b(z_{\text{cos}}) [1 + \delta_{\rho_{\text{HI}}}^s(\mathbf{s})]$ (i.e. Eq. 53), where ΔV^s is the total redshift-space volume of the cell, and $n_{\text{HI,cell}}^s = (1 + z_{\text{cos}})^3 (\sum \delta N_{\text{HI,sub}}) / \Delta V^s = (1 + z_{\text{cos}})^3 \Delta N_{\text{HI}} / \Delta V^s$ is the *cell-wise* (physical) HI number density in redshift space.

5.2.4 Spin Temperature Reloaded

In this subsection we generalize our calculation to the case of arbitrary spin temperature. Following the same algebra as in Section 5.2.3, for each unresolved subcell, $\delta T_b \delta V^s =$

¹⁵ Here $d_A(z) \equiv \frac{c}{H_0} |\Omega_k|^{-1/2} S \left[|\Omega_k|^{1/2} \int_0^z \frac{dz'}{E(z')} \right]$, where $E(z) \equiv \frac{H(z)}{H_0}$ is the relative cosmic expansion rate, and the function $S(x)$ equals $\sin(x)$ if $\Omega_k < 0$, x if $\Omega_k = 0$, and $\sinh x$ if $\Omega_k > 0$. Strictly speaking, it should be $d_A(z_{\text{cos}})$ that differs from $d_A(z_{\text{obs}})$ by $v_{\parallel}(1 + z_{\text{obs}})/H(z_{\text{obs}})$. Since d_A is large at high redshift, this difference is negligible.

$(1+z_{\text{cos}})^3 \frac{\widehat{\delta T}_b(z_{\text{cos}})}{\widehat{n}_{\text{HI}}(z_{\text{cos}})} \delta N_{\text{HI}} \left[1 - \frac{T_{\text{CMB}}(z_{\text{cos}})}{T_s^{r,\text{eff}}(\mathbf{r})} \right]$. Then the brightness temperature of a cell is

$$\delta T_b(\nu_{\text{obs}}) = \frac{\widehat{\delta T}_b(z_{\text{cos}})}{\widehat{n}_{\text{HI}}(z_{\text{cos}})} \left\langle n_{\text{HI}} \left[1 - \frac{T_{\text{CMB}}}{T_s^{\text{eff}}} \right] \right\rangle_{\text{cell}} \quad (54)$$

where

$$\left\langle n_{\text{HI}} \left[1 - \frac{T_{\text{CMB}}}{T_s^{\text{eff}}} \right] \right\rangle_{\text{cell}} = \frac{1}{\Delta V^s} \sum_{\text{subcells}} \left\{ n_{\text{HI}}^s(\mathbf{s}) \times \left[1 - \frac{T_{\text{CMB}}(z_{\text{cos}})}{T_s^{s,\text{eff}}(\mathbf{s})} \right] \delta V^s \right\}_{\text{sub}} \quad (55)$$

is the redshift-space-volume-weighted cell-wise average of $n_{\text{HI}} \left[1 - \frac{T_{\text{CMB}}}{T_s^{\text{eff}}} \right]$, or in other words, the cell-wise total of $\delta N_{\text{HI}} \left[1 - \frac{T_{\text{CMB}}}{T_s^{\text{eff}}} \right]$ per unit proper redshift-space volume. Here we implicitly assume that spin temperature is preserved from real- to redshift-space, i.e., $T_s^{s,\text{eff}}(\mathbf{s}) = T_s^{r,\text{eff}}(\mathbf{r})$.

5.2.5 Breakdown of the Analogy to Galaxy Surveys

From our results it is clear that the analogy to galaxy redshift surveys breaks down due to two effects: finite optical depth and finite spin temperature, as mentioned before in Sec. 4.

For the first case, when the IGM is optically thick to 21cm radiation, i.e., $\tau_{\nu_{\text{obs}}} \gtrsim 1$, the brightness temperature is not linear in $\tau_{\nu_{\text{obs}}}$ (see Eqn. 47), and the optical depth itself is affected by peculiar velocity through its dependence on spatial derivatives that are higher order than $dv_{\parallel}/dr_{\parallel}$ (see Eqns. 45 and 46). Consequently, the brightness temperature is no longer proportional to the neutral atom density in redshift space.

For the second case, e.g. at high redshifts where $T_s \gg T_{\text{CMB}}$ is not satisfied¹⁶, neutral atoms in the same redshift-space volume element contribute unequally to the brightness temperature due to their spatial variation in level population, i.e., emitters can have different luminosity. Thus the brightness temperature is no longer proportional only to the neutral atom density in redshift space. When the mapping from real- to redshift-space is single-valued, the proportionality between observed brightness temperature and neutral atom density in redshift-space is spoiled by the spatially-varying correction factor, $1 - T_{\text{CMB}}/T_s^{r,\text{eff}}(\mathbf{r})$, according to Eqns. (54, 55). However, in the more general case in which the mapping may be multi-valued, this correction factor is an average over the different real-space streams that contribute to the same redshift-space element, weighted by their different redshift-space neutral atom densities.

5.3 Redshift-space Distortion on 21cm Power Spectrum

The 21cm redshift-space-distorted power spectrum in the linear approximation was explored in Barkana & Loeb (2005), who showed

¹⁶ It is generally assumed that sufficiently late after the formation of the first stars, the spin temperature is well above the CMB temperature. This assumes, e.g., that the IGM is heated but only weakly ionized, as by the X-rays expected from early galaxies and mini-quasars (e.g. Chen & Miralda-Escudé 2004). It also assumes that the first stars produce a strong enough Ly α -pumping background to couple T_s to the kinetic temperature of the gas through the Wouthuysen-Field effect (e.g. Ciardi & Madau 2003). However, the length of the transition period from $T_s \lesssim T_{\text{CMB}}$ in the Dark Ages to $T_s \gg T_{\text{CMB}}$ during the later stages of the EOR is an unsettled topic (see, e.g., Baek et al. 2010).

that the linear 21cm power spectrum is distorted in a form analogous to the linear redshift space distortion in galaxy surveys. The authors computed the power spectrum of linearized peculiar-velocity-corrected 21cm brightness temperature, nevertheless, in *real* space, i.e. they linearized gas density, neutral fraction, and particularly the velocity gradient correction $1/(1 + \delta_{\partial_r,v}^r) \approx 1 - \delta_{\partial_r,v}^r$ by assuming $\delta_{\partial_r,v}^r \ll 1$, and computed the Fourier transform of the brightness temperature evaluated in real space. The observable power spectrum, however, is in redshift space. Although the expression of power spectrum derived in Barkana & Loeb (2005) can give correct values on large scales, this approach is conceptually incomplete. In addition, the assumption of $\delta_{\partial_r,v}^r \ll 1$ may break down on small scales. A further complication is that Barkana & Loeb (2005) assume that the product of neutral fraction fluctuation and the gas density fluctuation, $\delta_{x_{\text{HI}}} \delta_{\rho_{\text{H}}}$, can be neglected, which can be invalid and cause the power spectrum to become inaccurate with a fractional error at the 200% level when the universe is 50% ionized (Lidz et al. 2007).

In this section, we present a reformulation for computing the 21cm power spectrum in observer redshift space, taking into account both distortions in brightness temperature and in apparent location, and give the general equation for the linear redshift-space-distorted power spectrum without assuming either $\delta_{\partial_r,v}^r \ll 1$ or $\delta_{x_{\text{HI}}} \delta_{\rho_{\text{H}}} \ll 1$. Small optical depth is still assumed in the derivation.

Consider a slice $\delta T_b^s(\mathbf{s})$ of a 3D data cube near z_{cos} , in redshift space. The brightness temperature in Fourier redshift space is $\widehat{\delta T}_b^s(\mathbf{k}) \equiv \int d^3s e^{-i\mathbf{k}\cdot\mathbf{s}} \delta T_b^s(\mathbf{s})$. Since predictions of power spectra from theoretical modeling are made in real space, we should relate this redshift-space power spectrum to real-space quantities. The redshift- and real-space coordinates are related by Eqn.(6), and so the volume elements are related by $d^3s = d^3r [1 + \delta_{\partial_r,v}^r]$. The observed brightness temperature is preserved (Eqns. 50 and 51). As before, the velocity gradient corrections for the brightness temperature and the redshift-space volume element cancel and we find that the 21cm power spectrum in redshift space is given by

$$\widehat{\delta T}_b^s(\mathbf{k}) = \widehat{\delta T}_b(z_{\text{cos}}) \int d^3r e^{-i\mathbf{k}\cdot\mathbf{r}} [1 + \delta_{\rho_{\text{HI}}}^r(\mathbf{r})] \times \exp \left[-i \left(\frac{1+z_{\text{cos}}}{H(z_{\text{cos}})} \right) k_{\parallel} v_{\parallel}(\mathbf{r}) \right] \left[1 - \frac{T_{\text{CMB}}(z_{\text{cos}})}{T_s^{r,\text{eff}}(\mathbf{r})} \right], \quad (56)$$

where $k_{\parallel} = \mathbf{k} \cdot \hat{r}$.

5.3.1 Linear $\mu_{\mathbf{k}}$ -decomposition Scheme

Eqn.(56) is the general and exact equation to compute the 21cm power spectrum. In this subsection, we work out the linear case. In this we only take the density and velocity fluctuations to be linear, but the reionization fluctuations are allowed to be nonlinear. This means that we do not assume $\delta_{x_{\text{HI}}} \delta_{\rho_{\text{H}}} \ll 1$ and thus our approach is more general than that of Barkana & Loeb (2005). We therefore choose not to call it ‘‘linear theory’’, but instead introduce the new name *linear $\mu_{\mathbf{k}}$ -decomposition scheme*.

On large scales corresponding to small enough k so that $\left(\frac{1+z_{\text{cos}}}{H(z_{\text{cos}})} \right) k_{\parallel} v_{\parallel} \ll 1$, we can linearize the exponential and keep the linear term in v . We also linearize the spin-temperature-dependent term

$$\eta^r(\mathbf{r}) \equiv \left[1 - \frac{T_{\text{CMB}}(z_{\text{cos}})}{T_s^{r,\text{eff}}(\mathbf{r})} \right] \quad (57)$$

by defining its fluctuations as $\delta_{\eta}^r(\mathbf{r}) = [\eta^r(\mathbf{r}) - \bar{\eta}(z_{\text{cos}})] / \bar{\eta}(z_{\text{cos}})$

where $\bar{\eta}(z_{\text{cos}})$ is the mean value of η . We keep only the linear terms, and find $\widehat{\delta T_b^{s,\text{lin}}}(\mathbf{k}) = \widehat{\delta T_b}(z_{\text{cos}})\bar{\eta}(z_{\text{cos}}) \left[-i \left(\frac{1+z_{\text{cos}}}{H(z_{\text{cos}})} \right) k_{\parallel} \widetilde{v}_{\parallel}^r(\mathbf{k}) + \widetilde{\delta}_{\rho_{\text{HI}}}^r(\mathbf{k}) + \widetilde{\delta}_{\eta}^r(\mathbf{k}) \right]$. Here $\widetilde{a}^r(\mathbf{k}) \equiv \int d^3r e^{-i\mathbf{k}\cdot\mathbf{r}} a^r(\mathbf{r})$ is the Fourier transform of the quantity $a^r(\mathbf{r})$ in real space. On large scales, the velocity field is linear, $\widetilde{v}_{\parallel}^r(\mathbf{k}) = i \left(\frac{H(z_{\text{cos}})}{1+z_{\text{cos}}} \right) \widetilde{\delta}_{\rho_{\text{H}}}^r(\mathbf{k}) \frac{\mu_{\mathbf{k}}}{k}$, where $\mu_{\mathbf{k}} = k_{\parallel}/k$, $k = |\mathbf{k}|$, and $\widetilde{\delta}_{\rho_{\text{H}}}^r(\mathbf{k})$ is the total hydrogen density fluctuation in Fourier real-space. So we find

$$\widehat{\delta T_b^{s,\text{lin}}}(\mathbf{k}) = \widehat{\delta T_b}(z_{\text{cos}})\bar{\eta}(z_{\text{cos}}) \left[\widetilde{\delta}_{\rho_{\text{H}}}^r(\mathbf{k}) \mu_{\mathbf{k}}^2 + \widetilde{\delta}_{\rho_{\text{HI}}}^r(\mathbf{k}) + \widetilde{\delta}_{\eta}^r(\mathbf{k}) \right]. \quad (58)$$

The power spectrum in the linear $\mu_{\mathbf{k}}$ -decomposition scheme in redshift space, defined as $\left\langle \widehat{\delta T_b^{s,\text{lin}}}(\mathbf{k}) \widehat{\delta T_b^{s,\text{lin}}}(\mathbf{k}') \right\rangle \equiv (2\pi)^3 P_{\Delta T}^{s,\text{lin}}(\mathbf{k}) \delta^{(3)}(\mathbf{k} - \mathbf{k}')$, is

$$P_{\Delta T}^{s,\text{lin}}(\mathbf{k}) = P_{\mu,0}(k) + P_{\mu,2}(k) \mu_{\mathbf{k}}^2 + P_{\mu,4}(k) \mu_{\mathbf{k}}^4, \quad (59)$$

where the moments of $\mu_{\mathbf{k}}$ -polynomial expansion are

$$P_{\mu,0}(k) = \left(\widehat{\delta T_b} \bar{\eta} \right)^2 \left[P_{\delta_{\rho_{\text{HI}}, \delta_{\rho_{\text{HI}}}}^r}(k) + P_{\delta_{\eta}, \delta_{\eta}}^r(k) + 2P_{\delta_{\rho_{\text{HI}}, \delta_{\eta}}^r}(k) \right], \quad (60)$$

$$P_{\mu,2}(k) = 2 \left(\widehat{\delta T_b} \bar{\eta} \right)^2 \left[P_{\delta_{\rho_{\text{HI}}, \delta_{\rho_{\text{H}}}}^r}(k) + P_{\delta_{\eta}, \delta_{\rho_{\text{H}}}}^r(k) \right], \quad (61)$$

$$P_{\mu,4}(k) = \left(\widehat{\delta T_b} \bar{\eta} \right)^2 P_{\delta_{\rho_{\text{H}}, \delta_{\rho_{\text{H}}}}^r}(k), \quad (62)$$

where all quantities here depend implicitly on the redshift z_{cos} . Here $P_{a,a}^r$ denotes the auto power spectrum of the quantity $a^r(\mathbf{r})$, and $P_{a,b}^r$ is the cross power spectrum between fields $a^r(\mathbf{r})$ and $b^r(\mathbf{r})$, both in real space. Note that, strictly speaking, the power spectra involving δ_{η} are not statistically isotropic due to the distortion by peculiar velocity as in Eqn.(34). Since the correction is of order v/c , we ignore it here. When $T_s \gg T_{\text{CMB}}$, $\eta = 1$ and $\delta_{\eta} = 0$, and the power spectrum in linear $\mu_{\mathbf{k}}$ -decomposition scheme reduces to Eqn.(4).

Although we derived the scheme by assuming linear density and velocity fluctuations, when using it on simulation data, we normally use the non-linear density fluctuations given by the simulation.

As pointed out above, each moment of the $\mu_{\mathbf{k}}$ -decomposition can contain higher-order cross-correlations between density and ionization fraction, because $\delta_{\rho_{\text{HI}}}^r = \delta_{\rho_{\text{H}}}^r + \delta_{x_{\text{HI}}}^r + \delta_{\rho_{\text{H}}}^r \delta_{x_{\text{HI}}}^r$. However, we neglect the nonlinear coupling of peculiar velocity and reionization patchiness, which we will investigate in future work (Shapiro et al. 2011).

6 COMPUTATIONAL SCHEMES TO PREDICT BRIGHTNESS TEMPERATURE IN REDSHIFT SPACE

Analytical models and semi-numerical or numerical simulations provide us with *real*-space data. In order to make predictions for the observed 21cm power spectrum, we need to calculate the fully nonlinear 21cm brightness temperature accurately and efficiently in *redshift* space, accounting for all effects of peculiar velocities. In this section, we proposing two self-consistent computational schemes for this calculation. These two schemes are valid in the optically thin limit. Also, for simplicity, we assume that $T_s \gg T_{\text{CMB}}$ hereafter, but our schemes can be readily generalized to the arbitrary T_s case.

6.1 Real-to-Redshift-Space-Mapping (RRM) Schemes

As explained in Section 5.2.1, the effects of peculiar velocity can be separated into an effect on the observed brightness temperature and one on the apparent location of the 21cm emission source. So in principle, in order to compute the signal in redshift space, the brightness temperature should first be corrected by the velocity gradient, evaluated in real space, and then shifted to the apparent location corresponding to the Doppler frequency shift, with the volume element re-sized according to the velocity gradient, and finally re-sampled onto a regular grid in redshift space. This process is in general computationally cumbersome.

For 21cm tomography, however, we can exploit the proportionality between the 21cm brightness temperature and the neutral atom number density both measured in redshift space. Inspired by common wisdom in large-scale structure simulations, we propose two computational schemes based on mapping the neutral atom density from real- to redshift-space, and then computing the 21cm brightness temperature in redshift space using Eqn.(53).

6.1.1 Particle-to-Particle-to-Mesh (PPM)-RRM scheme

Most numerical simulations of reionization are processed as follows. First one runs a large-scale N-body simulation, from which one obtains gridded density fields and the collapsed halo information such as location and mass. The reionization simulation is then run on these gridded density fields using the halos as sources of radiation. Since the RT grid resolution is typically coarser than the N-body particle resolution, the most accurate 3D map of the neutral atom distribution in redshift space that can be possibly achieved from a given reionization simulation is made by taking advantage of the high-resolution N-body particle information. We propose the *Particle-to-Particle-to-Mesh Real-to-Redshift-Space-Mapping* (“PPM-RRM”) scheme as follows:

- We compute the bulk-flow velocity of the IGM at the position of particles directly from N-body particle data using an adaptive-kernel, SPH-like approach. The SPH-smoothed bulk velocity assigned to each particle is the smoothed momentum density divided by the smoothed mass density, evaluated at the particle location.¹⁷
- We assign each particle the neutral fraction from the RT grid cell that it is located in.
- For a given LOS direction, we Doppler-shift the N-body particles to their apparent locations according to the LOS bulk-flow velocity, in accordance to Eqn.(6).
- We compute new smoothing kernel lengths using the new particle positions in redshift-space.
- We use those kernel lengths to smooth the particle data (i.e. H I mass) onto a regular, redshift-space grid (see the discussion of grid resolution below). In this step, we exclude particles contained in halos¹⁸.

¹⁷ If a hydrodynamical simulation is coupled to N-body cold dark matter (CDM) simulation, then the gas particle velocity can be directly used. But since our simulations are dark matter only, we approximate the gas bulk-flow velocity as the SPH-smoothed velocity at the particle location (see Appendix A). One cannot use the particle velocities directly because those can be multi-streaming. In all this we assume that the gas traces the dark matter exactly, which is a good approximation on large scales.

¹⁸ We simulate the reionization of the IGM, and therefore compute the 21cm brightness temperature only from the IGM, so excluding particles in halos.

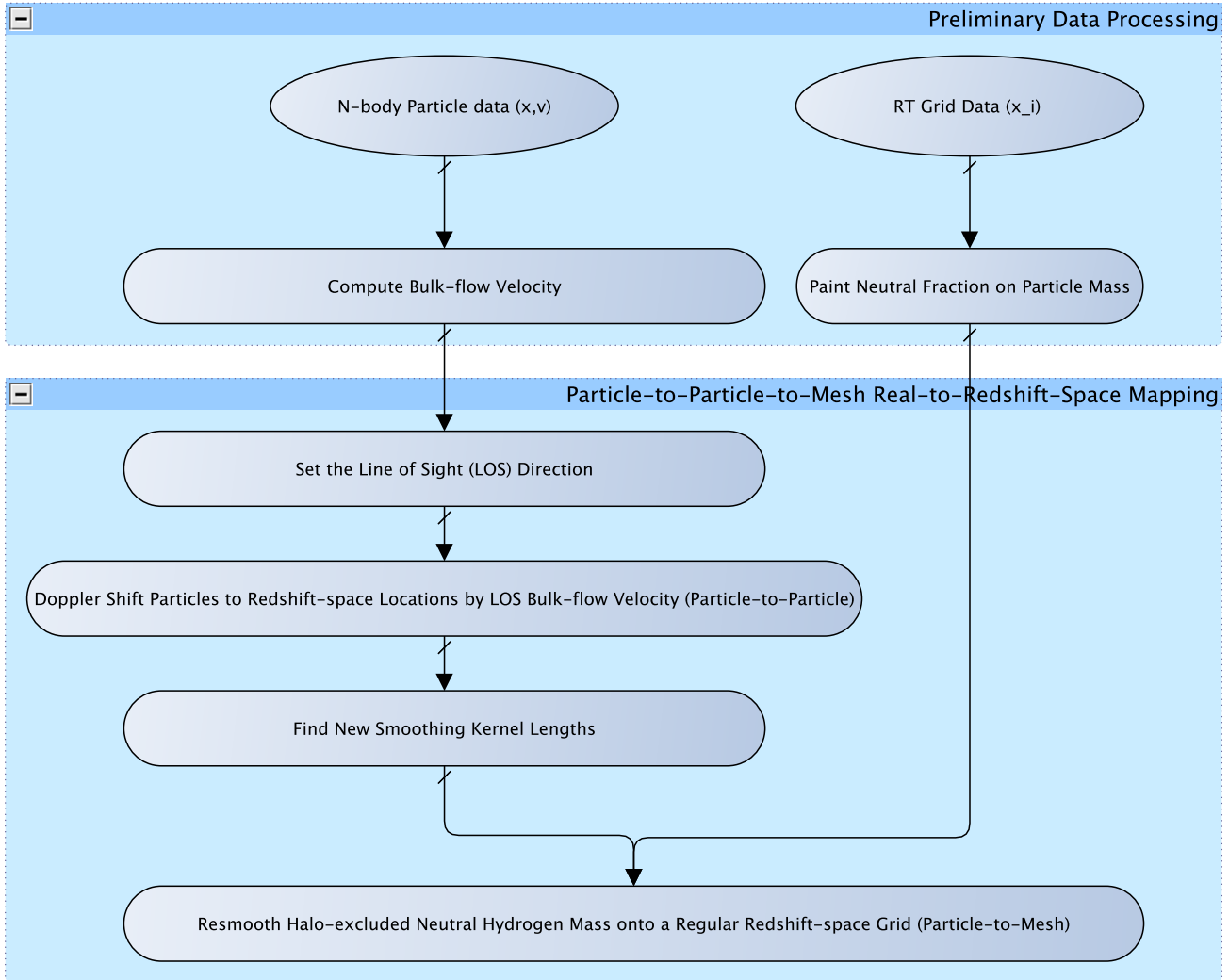


Figure 5. Flowchart of the PPM-RRM scheme.

- From this latter, gridded density field, we compute the HI density fluctuations in redshift-space, and from this the 21cm brightness temperature measured in redshift space using Eqn.(53).

Some details of the particle smoothing algorithm are discussed in Appendix A. We use adaptive kernels rather than fixed-kernels so as to better resolve the small scale spatial variations in overdense regions.

The high wavenumber modes in the power spectrum can be inaccurate due to sampling effects when calculating the power spectrum using the fast Fourier transform (FFT). Instead of correcting the power spectrum using the method proposed by Jing (2005), we partly avoid the sampling effect by gridding the particle data onto a redshift-space grid at four times higher resolution than the RT grid, but only keeping the modes in the power spectrum with $k \leq \pi/\Delta L$ (ΔL is the RT grid spacing), i.e. one-quarter of the Nyquist wavenumber for a grid with the resolution $\Delta L/4$. The reason for this and a summary of the sampling effect are discussed in more detail in Section 6.3.

The PPM-RRM prescription can be summarized as “ $P_r \rightarrow P_s \rightarrow M_s(4 \times RT)$ ” where “P” means particle data, “M” means mesh

data, subscript “r” means real-space, “s” means redshift-space, and “ $4 \times RT$ ” indicates that the grid resolution is 4 times finer than RT grid resolution. Fig. 5 shows the flow chart for the PPM-RRM scheme.

6.1.2 Mesh-to-Mesh(MM)-RRM scheme

Manipulating N-body particle data is accurate but computationally costly (see Table 1 below). Since the N-body particle data typically already have been smoothed onto a regular, real-space grid in order to simulate the radiative transfer, we propose an alternative scheme, the *Mesh-to-Mesh Real-to-Redshift-Space-Mapping* (“MM-RRM”) scheme. Mellema et al. (2006b) were actually the first to use the MM-RRM scheme to produce brightness temperature spectra and maps along the LOS (their Figs. 4, 9 and 10), but did not provide a detailed description of the method in their paper. This scheme saves computational resource by using the real-space grid data such as cell-wise mass density, velocity, and ionization fraction, but gives consistent results (depending on the grid resolu-

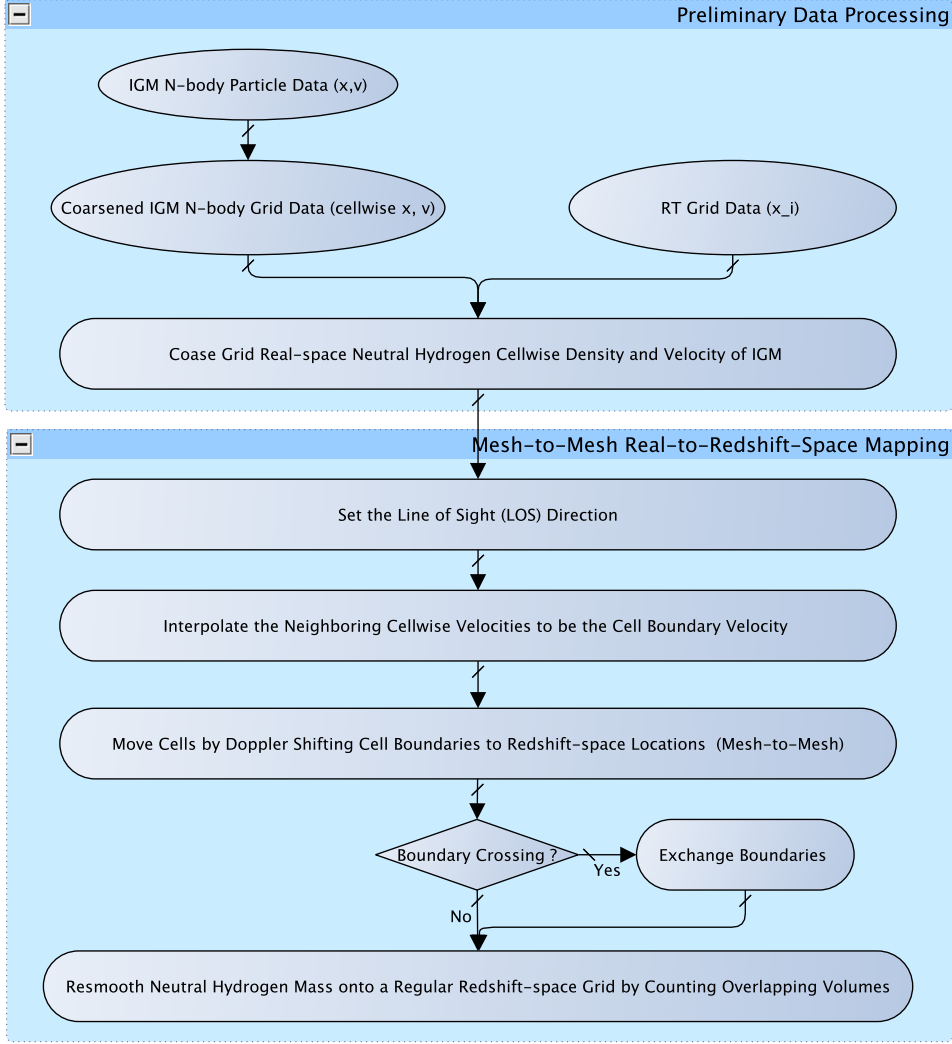


Figure 6. Flowchart of the MM-RRM scheme.

tion, to be tested in Section 6.5). The MM-RRM scheme works as follows:

- As the preliminary step, we grid the N-body particle data in the IGM (i.e. particles in the halo excluded) onto a regular, real-space grid with a resolution n times finer than the RT resolution, using our adaptive kernel SPH-like smoothing. This provides us with cell-wise density and velocity fields.

- We assign each cell the neutral fraction from the RT grid that this fine cell belongs to.

- We assume the cell-wise velocity to be the velocity at the cell center, and compute the LOS velocity at the boundary between two LOS-neighboring cells by linear interpolation.

- We shift the cell boundaries to their apparent locations according to their LOS velocity, in accordance with Eqn. (6), whereby the real-space cell can get stretched or compressed in redshift space. In high density cells the boundaries of a cell can cross each other in redshift space, an effect known as the *finger of God*. When this happens, we switch the cell's crossing boundaries so that the cell size is always positive.

- We regrid the neutral hydrogen mass from the real-space grid

onto a regular, redshift-space grid at the same resolution, by counting the overlapping volumes; e.g., if the LOS is along the x -axis, a real-space cell (i, j, k) with the size Δx stretches to the length $\Delta x'_i$ in redshift-space, with a portion of this length, $\Delta L_{i,i'}$, overlapping the cell (i', j, k) in the regridded, redshift-space, mesh, then all real-space cells (i, j, k) contribute to the neutral hydrogen density of the redshift-space cell (i', j, k) , according to

$$\rho_{\text{HI}}^s(i', j, k) = \sum_i F_{i,i'} \rho_{\text{HI}}^r(i, j, k), \quad (63)$$

where $F_{i,i'}$ is the fractional overlap of the real-space volume i with the redshift-space volume i' , i.e. $F_{i,i'} = \Delta L_{i,i'} / \Delta x'_i$ (the indices j and k are not relevant here because we move all cells along the x -axis).

- We compute the HI density fluctuations in redshift-space, and from this the 21cm brightness temperature using Eqn.(53). This is done at n times higher resolution than the RT grid, but when calculating the power spectrum we only keep modes with $k \leq \pi / \Delta L$ (ΔL is the RT grid spacing).

The MM-RRM scheme can be summarized as “[$P_r \rightarrow M_r(n \times RT)$] $\rightarrow M_s(n \times RT)$ ”, where the operation inside the square bracket is the prerequisite step. In Section 6.5 we will experiment with different resolution factors n to find the optimal resolution. Fig. 6 shows the flow chart for the MM-RRM scheme.

6.1.3 The Redshift-space-distorted Lightcone Effect

Both the PPM-RRM and MM-RRM schemes deal with simulation data from a finite volume at a fixed cosmic time, implicitly assuming that the cosmic evolution of both neutral fractions and density perturbations are negligible during the light travel time across the simulation box, t_{cross} . For the typical simulation volume sizes (100-200 Mpc) one does not expect much evolution in the density field during t_{cross} . However, the neutral fractions may evolve much more rapidly during some periods of the EoR. If $(d \ln x_i / dt) \delta t \gtrsim 1$, then we must take into account this so-called lightcone effect (Barkana & Loeb 2006) and couple it to peculiar velocity. This implies first time-interpolating the particle data to the appropriate look back time and the corresponding real-space location and then shifting the particles to their apparent location according to its interpolated LOS peculiar velocity, and finally mapping these time interpolated particles onto a regular redshift-space grid on the lightcone. The full version of the lightcone PPM-RRM scheme is beyond the scope of this paper¹⁹ and we postpone an investigation of this effect to a future paper in this series.

6.2 Simulations

For our reionization simulation we use a new large-scale, high-resolution N-body simulation of the Λ CDM universe (performed with the CubeP³M code, Iliev et al. 2008b) in a comoving volume of $L_{\text{box}} = 114 \text{ Mpc}/h$ on each side using 3072^3 (29 billion) particles. To find the halos, we use the spherical overdensity method and require them to consist of at least 20 N-body particles; this implies a minimum halo mass of $10^8 M_\odot$.

Assuming that the gas traces the CDM particles exactly, we grid the density on a 256^3 grid using SPH-like smoothing with an adaptive kernel. The halo lists and density fields are then processed with the radiative transfer code C²Ray (Mellema et al. 2006a). Each halo releases f_γ ionizing photons per baryon per $\Delta t = 11.5 \text{ Myrs}$, with $f_\gamma = 150$ ($f_\gamma = 10$) for halos below $10^9 M_\odot$ (above $10^9 M_\odot$), respectively. To incorporate feedback from reionization, halos less massive than $10^9 M_\odot$ located in ionized regions are not producing any photons.

The simulations were run on the University of Texas Sun Constellation Linux Cluster *Ranger*, one of the largest computational resources in the world. Both codes are massively parallel, using 512 compute nodes, each with one Quad-Core 64-bit processor. We refer the readers to Friedrich et al. (2010) and Iliev et al. (2011) for more details of this simulation which in those papers is labelled as “163Mpc_g8.7_130S”.

The simulations used the following set of cosmological parameters $\Omega_\Lambda = 0.73$, $\Omega_M = 0.27$, $\Omega_b = 0.044$, $h = 0.7$, $\sigma_8 = 0.8$, $n_s = 0.96$ where $H_0 = 100h \text{ km s}^{-1} \text{ Mpc}^{-1}$, consistent with the *WMAP* seven-year results (Komatsu et al. 2011).

¹⁹ Mellema et al. (2006b) *did* apply such a time interpolation of *grid* data, both on the neutral fraction and density fields.

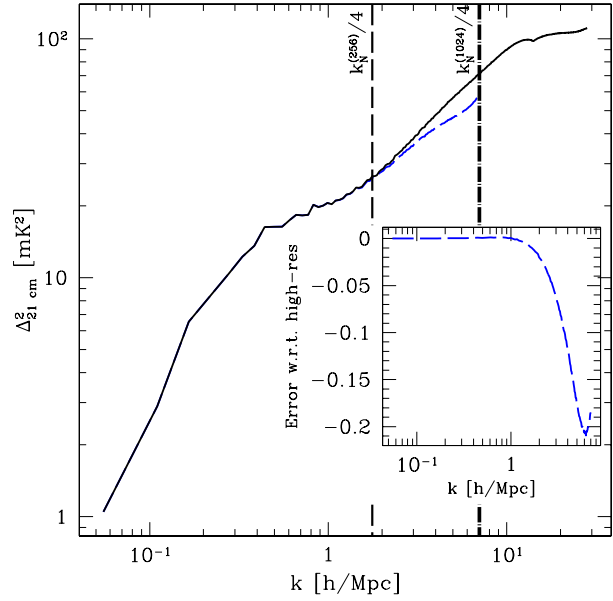


Figure 7. Aliasing effect in the PPM-RRM scheme: 21cm redshift-space 1D power spectrum at $z = 9.457$ (50% ionized), when the particle data is smoothed onto a regular, redshift-space, grid with the RT grid resolution (256^3 , long-dashed, blue), or four times finer (1024^3 , solid, black). The vertical lines are at $k = k_N^{(256)}/4 = 1.75 \text{ h/Mpc}$ (thin long-dashed) and $k = k_N^{(1024)}/4 = k_N^{(256)}/4 = 7 \text{ h/Mpc}$ (thick dot-long-dashed), respectively. The fractional error plotted in the inset is with respect to the power from the 1024^3 grid.

6.3 Sampling Effects

Measuring power spectra using a fast Fourier transform (FFT) of gridded data suffers from the so-called *sampling effect*. This effect is due to the mass assignment of particle data or continuous fields to a chosen grid. In cosmology, it was first extensively discussed for power spectrum measurements of density fields in large scale structure (see, e.g., Jing 2005, Cui et al. 2008, and references therein). The mass assignment is equivalent to convolving the true density field with a window function and sampling this convolved density field with a finite number of grid points. The power spectrum of the convolved field is a *biased* one, i.e., (Jing 2005)

$$P^f(\mathbf{k}) = \sum_{\mathbf{n}} \left| \tilde{W}(\mathbf{k} + 2k_N \mathbf{n}) \right|^2 P(\mathbf{k} + 2k_N \mathbf{n}) + P_{\text{shot}}, \quad (64)$$

where $P^f(\mathbf{k})$ and $P(\mathbf{k})$ are power spectra of the convolved and true field, respectively, $\tilde{W}(\mathbf{k})$ is the Fourier transform of the window function, P_{shot} is the shot noise, and the summation is over all three-dimensional integer vectors \mathbf{n} . The sampling effects include three aspects that can affect the true power spectrum measurement (Cui et al. 2008).

- Smoothing effect: the Fourier window function $|\tilde{W}(\mathbf{k})|^2$ falls off sharply from $|\tilde{W}(\mathbf{0})|^2 = 1$, e.g., for a Cloud-In-Cell (CIC) window function, $|\tilde{W}|^2 = 0.90$ at $k = k_N/4$, but $|\tilde{W}|^2 = 0.66$ at $k = k_N/2$, where $k_N = \pi/a$ is the Nyquist wavenumber for some grid spacing a .
- Anisotropy effect: the Fourier window function is not isotropic for a given k , and the anisotropy is significant for $k \sim k_N$.
- Aliasing effect: higher wavenumber modes ($\mathbf{n} \neq 0$) contaminate the true mode at \mathbf{k} , preventing us from relating $P^f(\mathbf{k})$ and

$P(\mathbf{k})$ straightforwardly. For a FFT, $(-k_N, k_N)$ is the range in \mathbf{k} -space that a finite resolution grid can probe. Thus those high-wavenumber modes that contaminate are due to modes of the unresolved field below the grid resolution.

The smoothing effect and anisotropy effect can easily be corrected for, e.g. by just deconvolving $P^f(\mathbf{k})$ with the normalization $|\tilde{W}(\mathbf{k})|^2$. Correcting the aliasing effect is more difficult, and may be done using the iterative method proposed and tested for the density power spectrum by Jing (2005). Instead, we can be less ambitious and define a ‘‘comfort’’ zone ($k \lesssim$ some critical value) where the FFT power spectrum has negligible errors. This can be done because at low enough k , all these sampling effects should be insignificant. The test problems in both Jing (2005) and Cui et al. (2008) seem to agree that the raw density power spectra for different window functions agree at $k \lesssim k_N/4$. Here we test this on the 21cm power spectrum. In Fig. 7 we compare two power spectra, both calculated with the PPM-RRM scheme but differing in the resolution chosen for gridding the redshift-space particle data, 256^3 and 1024^3 , respectively. As can be seen in the figure, both power spectra agree for $k \lesssim k_N^{(256)}/4$, where $k_N^{(256)}$ is the Nyquist wavenumber of the 256^3 grid. We therefore conclude that if we use the 256^3 grid, we can trust the results for $k \lesssim k_N^{(256)}/4$.

However, this comparison also shows that we can use our high-resolution N-body data to try to capture the modes between $k = k_N^{(256)}/4$ and $k = k_N^{(1024)}$. By sampling the Doppler-redshifted particle data onto a grid with a resolution of $4 \times \text{RT} = 1024^3$ we can minimize the smoothing and anisotropy effects. We also minimize the aliasing effect due to the gridded density and velocity data. The aliasing effect due to the finite resolution of the ionization fraction field obviously cannot be corrected for this way. However, this effect may be quite small due to the nature of the ionization fraction field. Recall that the aliasing effect is due to the contamination from high-wavenumber modes unresolved by the grid resolution. For blackbody type sources, the edges of ionized regions are sharp, i.e. the ionization fraction is very close to 1 inside and very nearly 0 outside ionized regions. Therefore only cells that contain boundaries of ionized regions have unresolved subcell information. The fraction of boundary cells for an ionized region of N cells in each dimension is $\sim N^2/N^3 = 1/N$. Typical large bubble sizes can be ~ 10 Mpc corresponding to ~ 22 RT cells across a bubble (see, e.g. Friedrich et al. 2010). For such bubbles only $\sim 4\%$ of the cells contribute to the aliasing effect. Only if there are many small bubbles of size less than a RT cell, would the ionization field introduce a substantial aliasing effect.

Given this argument it would seem prudent to choose the smoothed grid resolution to be four times smaller than the RT resolution, as this minimizes the sampling effects for the 21cm power spectra. We therefore adopt this approach. The modes between $k_N/4$ and k_N (where k_N here corresponds to RT grid resolution) may still be affected by the aliasing effect due to the finite RT grid resolution, but we expect this to be a minor effect.

6.4 Tests of PPM-RRM Scheme

Since the PPM-RRM ($4 \times \text{RT}$) scheme retains the particle data the longest by mapping them directly into redshift space, it can be expected to be more accurate than the MM-RRM scheme. We therefore first present tests for the PPM-RRM scheme in this section and in the next section compare the results of the two schemes.

6.4.1 Conservation of Mass

The mean total (and neutral) hydrogen density is conserved between real- and redshift-space, because (i) the total (and neutral) hydrogen atom number is conserved, and (ii) the total space is conserved for a volume large enough (peculiar velocity vanishes for large distances) or a periodic box, since $\int \delta V^r \delta_{\partial_r, v}^r(\mathbf{r})$ is a total derivative.

For the simulation box, the total volume is automatically conserved. We can therefore check whether our schemes conserve mass by checking the conservation of mean hydrogen density and HI density. Conservation of the mean density could be violated if a scheme would undercount particles after shifting particles to redshift-space.²⁰

Our code passes this test by showing that the fractional differences of the mean total (and neutral) hydrogen density between real-space and redshift-spaces with three distinct LOS directions are zero, i.e. smaller than machine error.

6.4.2 Large Scale Test

As shown in Section 5.3, the fully nonlinear power spectrum reduces to the $\mu_{\mathbf{k}}$ -decomposition power spectrum at large scales. We use this here to test the PPM-RRM scheme. Fig. 8 (top panels) shows the 1D dimensionless²¹ power spectrum $\Delta_{21\text{cm}}^2(k) = k^3 P_{\Delta T}^s(k)/2\pi^2$ calculated with the PPM-RRM scheme. In order to minimize noise, we averaged the power spectra for three distinct LOS directions (namely, along x -, y - and z -axes). Plotted in the same figure is the 1D $\mu_{\mathbf{k}}$ -decomposition power spectrum calculated directly from the real-space ionization fraction (on the 256^3 grid) and density and velocity data (on the 1024^3 grid), using Eqns.(59 - 62). We choose the 50% ionized epoch for this comparison. Note that even though we use the linear $\mu_{\mathbf{k}}$ -decomposition scheme equations to evaluate the power spectrum, we use the fully nonlinear density and ionization fraction fields from the simulation.

The comparison shows that the nonlinear power spectrum computed from the PPM-RRM scheme agrees with the $\mu_{\mathbf{k}}$ -decomposition power spectrum at large scales ($k \lesssim 0.3 h/\text{Mpc}$) within 5%. This confirms that the 21cm brightness temperature data cube constructed by the PPM-RRM scheme captures the correct large-scale fluctuations in redshift space as dictated by the linear $\mu_{\mathbf{k}}$ -decomposition scheme. The nonlinear power spectrum deviates from the linear $\mu_{\mathbf{k}}$ -decomposition power spectrum at intermediate scales ($0.3 \lesssim k \lesssim 2 h/\text{Mpc}$) at the level of $\sim 10\%$, and even larger deviations can be found at smaller scales. In the second paper of this series (Shapiro et al. 2011), we will investigate in detail the

²⁰ To parallel-process N-body particle data using Message Passing Interface (MPI) software, the simulation volume is divided into cubic partitions and particles are assigned to the partition within which they are located. Each partition is processed independently by a given node in the parallel computer. The mapping described here of particle locations from real- to redshift-space can move a particle out of its original (real-space) partition into another, even to one which is not a neighbor partition. In that case, the number of partition pairs that must share particle data, to exchange particles, can be large and, hence, computationally inefficient. Fortunately, we find that the size of each partition in our N-body simulations (which we also use for our real- to redshift-space mapping) is larger than the maximum Doppler shift of particles in comoving coordinates, so only neighboring partitions need exchange particle data.

²¹ It still has the unit mK^2 . It is dimensionless with regard to Fourier space units.

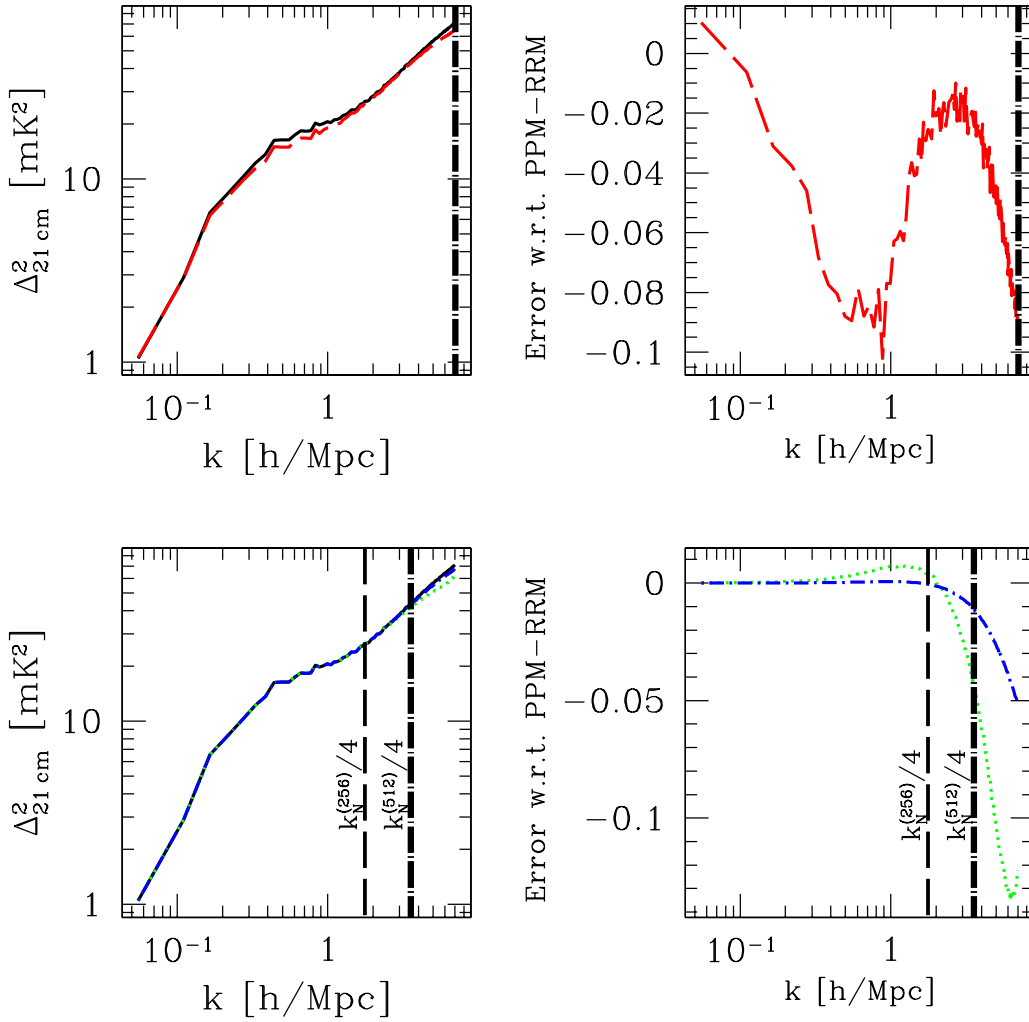


Figure 8. Tests of the PPM-RRM scheme for the 21cm redshift-space 1D power spectrum at $z = 9.457$ (50% ionized). Top panels: large scale test of the PPM-RRM scheme (solid, black) against the linear $\mu_{\mathbf{k}}$ -decomposition scheme (long-dashed, red), both computed from a 1024^3 grid, and Fourier modes kept only at $k \leq k_N^{(1024)}/4 = k_N^{(256)} = 7$ h/Mpc (the thick vertical lines). The fractional error is that of the linear $\mu_{\mathbf{k}}$ -decomposition scheme result with respect to the PPM-RRM result.

Bottom panels: small scale test of the PPM-RRM scheme computed from 1024^3 grid (solid, black) against the *DEMRF* scheme, computed on a 256^3 grid (dotted, green) and on a 512^3 grid (dot-short-dashed, blue), respectively. We only keep modes $k \leq k_N^{(256)} = 7$ h/Mpc. The black and blue curves are almost indistinguishable until at the very large k in the left bottom panel. The fractional errors are with respect to the PPM-RRM result. The vertical lines at $k = k_N^{(256)}/4 = 1.75$ h/Mpc (thin long-dashed) and $k = k_N^{(512)}/4 = 3.5$ h/Mpc (thick dot-long-dashed) delimit the comfort zone for the *DEMRF* result computed on a 256^3 and 512^3 grid, respectively.

cause of this departure from linearity and how it affects the use of 21cm observations for cosmology.

6.4.3 Test Down to Small Scales

Similar to the linear $\mu_{\mathbf{k}}$ -decomposition scheme test that employs the real-space grid data to compute the redshift-space statistics, we can compute the redshift-space power spectrum at all scales, in principle, by evaluating the integral in Eqn.(56). The integration can be carried out by a fast Fourier transform of the data cube $F(\mathbf{r}) = \exp\left[-i\left(\frac{1+z_{\text{cos}}}{H(z_{\text{cos}})}\right)k_{\parallel}v_{\parallel}(\mathbf{r})\right] \cdot [1 + \delta_{\rho_{\text{HI}}}^*(\mathbf{r})]$ (assuming $T_s \gg T_{\text{CMB}}$) for any given k_{\parallel} , and then picking up

only those modes with the LOS component k_{\parallel} , i.e., $\widetilde{\delta T_b^s}(\mathbf{k}) = \widetilde{\delta T_b(z_{\text{cos}})} \widetilde{F}(\mathbf{k})$ only if $\mathbf{k} \cdot \hat{n} = k_{\parallel}$. We can construct the whole Fourier data cube by making such FFT evaluation for each \mathbf{k} -space plane of constant $k_{\parallel} \geq 0$, exploiting the symmetry $\widetilde{\delta T_b^s}(-\mathbf{k}) = \widetilde{\delta T_b^s}^*(\mathbf{k})$, with k_{\parallel} discretized in units of $2\pi/L_{\text{box}}$.

Note that in order for the discrete Fourier transform to be a good approximation to the continuous Fourier transform, the particle data should in principle be smoothed to compute the cell-wise average $\langle F(\mathbf{r}) \rangle_{\text{cell}}$ and in particular $\left\langle \exp\left[-i\left(\frac{1+z_{\text{cos}}}{H(z_{\text{cos}})}\right)k_{\parallel}v_{\parallel}(\mathbf{r})\right] \right\rangle_{\text{cell}}$ directly. However, to take advantage of existing cell-wise density and velocity data on

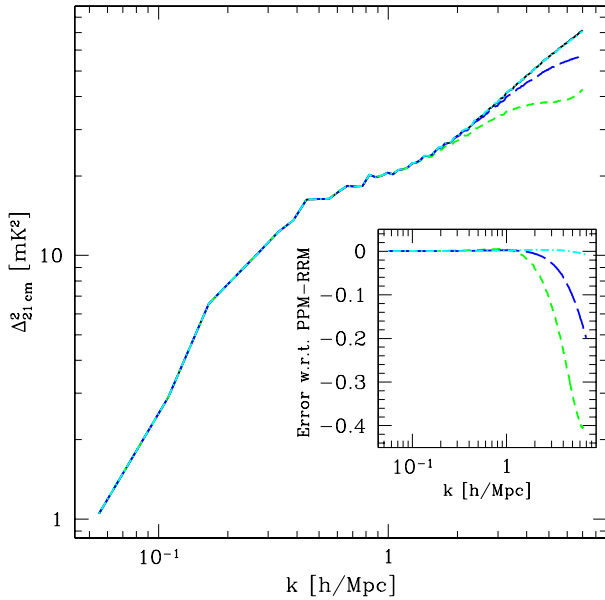


Figure 9. Test of the MM-RRM scheme: 21cm redshift-space 1D power spectrum at $z = 9.457$ (50% ionized). We experiment with grids of the RT grid resolution (short-dashed, green), 2 times (long-dashed, blue), and 4 times higher resolution (dot-short-dashed, cyan). The benchmark is the result from the PPM-RRM (4×RT) scheme (solid, black). The power spectra of the MM-RRM (4×RT) scheme and the PPM-RRM (4×RT) scheme are indistinguishable on all scales shown. The fractional errors of the MM-RRM results with respect to the PPM-RRM result are shown in the inset.

the grid, we evaluate $\left\langle \exp \left[-i \left(\frac{1+z_{\text{cos}}}{H(z_{\text{cos}})} \right) k_{\parallel} v_{\parallel}(\mathbf{r}) \right] \right\rangle_{\text{cell}} \rightarrow \exp \left[-i \left(\frac{1+z_{\text{cos}}}{H(z_{\text{cos}})} \right) k_{\parallel} \langle v_{\parallel}(\mathbf{r}) \rangle_{\text{cell}} \right]$. We compute the 1D power spectrum from the Fourier modes, averaged over three independent LOS directions. We name this method of evaluating the power spectrum the *Direct Evaluation by Multiple Real-space FFTs* (DEMRF) scheme.

Obviously, the DEMRF scheme is accurate only when the cell size is not too small so that $\langle v_{\parallel}^n(\mathbf{r}) \rangle_{\text{cell}} \approx \langle v_{\parallel}(\mathbf{r}) \rangle_{\text{cell}}^n$ for any $n > 1$ in the Taylor expansion of $\left\langle \exp \left[-i \left(\frac{1+z_{\text{cos}}}{H(z_{\text{cos}})} \right) k_{\parallel} v_{\parallel}(\mathbf{r}) \right] \right\rangle_{\text{cell}}$. On the other hand, if the grid is too coarse, the high- k powers are subject to the sampling effect and become inaccurate. We experiment on the trade-off by trying out the DEMRF scheme on grid data with different resolutions (256^3 , 512^3 and 1024^3), and find that for a box of size $114 \text{ Mpc}/h$, the 1024^3 grid is too fine and fails to make sensible results due to the subcell nonlinearity. We plot the DEMRF result computed from 256^3 and 512^3 grids in Fig. 8 (bottom panels), and find that within the comfort zone for each grid ($1.75 \text{ Mpc}/h$ and $3.5 \text{ Mpc}/h$, respectively), the PPM-RRM result agrees with the DEMRF results within 1%.

The three tests presented thus show that the PPM-RRM (4×RT) scheme is accurate on both large and small scales. We can now use this to test our other scheme.

6.5 Test of MM-RRM Scheme

The MM-RRM scheme is expected to be less accurate than the PPM-RRM scheme since it grids the particle data before moving to redshift space and inevitably small scale information is lost in

the process. For example, the gas density within a RT cell is assumed to be uniform, so that the resized cell in redshift-space can be uniformly regridded by counting overlapping volumes. This assumption obviously ignores the subcell clumpiness. Second, the scheme treats the velocity of cell boundary as the linear interpolation between cell-wise velocities of two neighboring cells and thus ignores small-scale velocity fluctuations at the inter-cell scale. Third, the treatment of cell boundary crossing is approximate and a careful treatment should require particle data to mimic the *finger of God* effect. However, the scales that are affected depend on the resolution chosen, and if one can choose a grid with fine enough resolution, there is a hope that the MM-RRM scheme can yield as accurate power spectra at $k \leq k_N$ (corresponding to RT grid resolution) as the PPM-RRM scheme does.

We experiment with the resolution of the MM-RRM scheme by choosing $n = 1, 2$ or 4 in the pipeline “[$P_r \rightarrow M_r(n \times \text{RT})$] → [$M_s(n \times \text{RT})$]” (where $n \times \text{RT}$ means the grid resolution n times finer than RT grid resolution). We compute the 21cm power spectrum for each of these three resolutions and plot them for the modes $k \leq k_N^{(256)}$ in Fig. 9. As above we average over three LOS directions. We use the PPM-RRM(4×RT) result as a benchmark. All MM-RRM results agree with the PPM-RRM result down to the scale $k \lesssim 1 \text{ h}/\text{Mpc}$, while at high k the MM-RRM(1×RT) and (2×RT) results deviate from the benchmark by up to 40% and 20%, respectively. Fortunately, the MM-RRM(4×RT) result agrees with the benchmark within 1% accuracy on all scales down to $k \leq k_N^{(256)}$. We therefore conclude that MM-RRM(4×RT) gives as accurate results as the PPM-RRM(4×RT) scheme for $k \leq k_N$.

7 PROBLEM WITH “ ∇v -LIMITED” PRESCRIPTION

Santos et al. (2010) treated the effects of peculiar velocity on the 21cm signal by using an equation equivalent of our Eqn. (36), an approach also adopted by 21cmFAST (Mesinger, Furlanetto & Cen 2011). As we have shown above, this equation gives the 21cm signal in *real-space*, not in observed redshift-space, and thus neglects the apparent location distortions²².

In addition, by using Eqn. (36), one is faced with the problem that the 21cm brightness temperature diverges when $\delta_{\partial_r v} \rightarrow -1$. Santos et al. (2010) and Mesinger, Furlanetto & Cen (2011) deal with this by imposing a minimum value larger than -1 for the calculated value of $\delta_{\partial_r v}$ (e.g., -0.7 in Santos et al. 2010, and -0.5 in Mesinger et al. 2011). We will name this approach the *∇v -limited prescription*. The argument for this ad hoc solution is that imposing this limit only affects a very small number of cells, and thus has no influence on global statistics such as the power spectrum. It is this argument that we want to investigate here.

7.1 Non-physical nature of the divergence “problem”

Before analyzing the accuracy of the ∇v -limited prescription, we would like to explain why the divergence encountered for $\delta_{\partial_r v} \rightarrow -1$ is a mathematical one but not a physical one.

The first part of this explanation was already considered in

²² It seems that the reason for neglecting to take into account these distortions (see e.g. footnote 7 of Mesinger, Furlanetto & Cen 2011) is that the apparent location distortion in redshift-space and the brightness temperature distortion in real-space were considered to be equivalent. As we have shown above this is incorrect.

Section 5.1.5. As we showed there, the locations at which $\delta_{\partial_r v} \rightarrow -1$ cannot be considered to be optically thin, and Eqn. (36) was derived under the assumption of low optical depth. When considering the optically thick case with thermal broadening, no divergence is found for $\delta_{\partial_r v} \rightarrow -1$.

However, even if one chooses to ignore optical depth effects, then the divergence in real-space does not correspond to a divergence in redshift-space. The reason is simply that real-space regions for which $\delta_{\partial_r v} \rightarrow -1$ become infinitesimally small in redshift-space, since $d^3s = d^3r |1 + \delta_{\partial_r v}^r(\mathbf{r})|$. This, of course, makes perfect sense since the 21cm brightness temperature produced by a region of space is proportional to the number of neutral hydrogen atoms in that region, which is always finite and is conserved by the mapping from real- to redshift-space (see also Section 5.2.3).

7.2 Is the “ ∇v -limited” prescription accurate?

The “ ∇v -limited” prescription (Santos et al. 2010) attempts to avoid the divergence problem by imposing a lower limit for $\delta_{\partial_r v}(\mathbf{r})$ when evaluating the brightness temperature using Eqn. (36), and then computing the power spectrum (in real space). Although the lower limit removes the divergence, this prescription contains a conceptual artifact (truncation of an unphysical divergence) and is incomplete (calculating the power spectrum in real- instead of redshift-space). In addition, the results may be sensitive to the chosen value for the lower limit. In this subsection, we test the ∇v -limited prescription by comparing it to the results of our PPM-RRM ($4 \times \text{RT}$) scheme.

In order to find gridded values for the velocity gradient, we use SPH-like smoothing of our N-body particle data to compute the velocity gradient. Details of this technique are discussed in Appendix A. We implement the ∇v -limited prescription by imposing the cap $\langle \delta_{\partial_r v} \rangle_{\text{cell}} \geq -\lambda$ at $\lambda = 0.5, 0.7, 0.9$, and 0.99 , evaluating and Fourier transforming the brightness temperature in real space. We average the power spectra over three LOS directions.

To most clearly show the effects of the ∇v -limited prescription we first take our volume to be fully neutral, by setting $x_{\text{HI}} = 1$ everywhere. Fig. 10 (left panel) shows the power spectra from the ∇v -limited prescription for four different values of the lower limit λ as well as the power spectrum calculated with the PPM-RRM scheme. We find that different values for λ yield rather different power spectra even on large scales, and none of these is consistent with the PPM-RRM result.

This is of course the most extreme case since in a fully neutral medium all locations with $\delta_{\partial_r v} \rightarrow -1$ contribute. Since these regions are preferably located in high density areas, which typically reionize earlier, one can expect that the effect is much less severe when considering a neutral fraction distribution obtained from a reionization calculation. Fig. 10 (right panel) shows this indeed to be case. On large scales, different limits in the ∇v -limited prescription yield converging power spectra which, however, have an offset of $\sim 25\%$ from the power spectrum of the PPM-RRM scheme. This offset is due to the enhancement in the mean brightness temperature averaged in real space, i.e. although the distribution of $\delta_{\partial_r v}(\mathbf{r})$ has zero mean, the distribution of $(1 + \delta_{\rho_{\text{HI}}}(\mathbf{r})) / |1 + \delta_{\partial_r v}(\mathbf{r})|$ does not have the (volume-weighted) mean of unity²³ due to the nonlin-

²³ This can be compared to the mean in redshift space, where the averaging is over redshift-space volume elements $d^3s = d^3r |1 + \delta_{\partial_r v}^r(\mathbf{r})|$, equivalent to averaging in real-space weighted by $|1 + \delta_{\partial_r v}^r(\mathbf{r})|$, and therefore the

ear function $1/|1 + \delta_{\partial_r v}|$. Although converged on large scales, on small scales the results of the ∇v -limited prescription still depend on the lower limit chosen and can have errors as large as 50% for $\lambda = 0.5$ (the cap adopted by Mesinger, Furlanetto & Cen 2011), 100% for $\lambda = 0.7$ (the cap adopted by Santos et al. 2010), and more divergent for larger caps. However, these errors are substantially smaller than the ones found for the fully neutral case.

Recall from Section 5.1.5 that thermal broadening can relax the singularity in the optical depth. One may therefore wonder whether imposing a lower limit on the velocity gradient can be considered as equivalent to introducing thermal broadening. The results in Fig. 10(b) show that this is not the case. The lower limit needed to be most consistent with the the PPM-RRM result is -0.5 . When $\delta_{\partial_r v} \sim -0.5$, the optical depth is no longer singular, in which case the thermal broadening only contributes to the optical depth at the level of 10^{-7} (see Section 5.1.4). Therefore, the limit imposed on the velocity gradient is not physically equivalent to the limiting of the optical depth due to thermal broadening.

In addition, even though the ∇v -limited prescription was invented to circumvent the unphysical divergence in 21cm brightness temperature in real-space regions that are optically thick to 21cm radiation, the cells that are affected by imposing a cap on velocity gradient are actually much more numerous than the optically-thick cells; e.g., at 50% ionized epoch in our simulation, we find that only a fraction of $\sim 10^{-7}$ amongst all cells are optically thick in the best case ($T_s/T_{\text{CMB}} = 100$), or $\sim 0.01\%$ in the worst case ($T_s/T_{\text{CMB}} = 0.1$), (see Section 5.1.6), but the ∇v -limited prescription affects $\sim 1\%$ of total cells in which $\delta_{\partial_r v} \leq -0.7$, or a fraction of $\sim 3\%$ with $\delta_{\partial_r v} \leq -0.5$. (These specific fractions can depend on the grid resolution of the simulation.) In other words, the ∇v -limited prescription affects a lot more cells than necessary.

The results in this section show that the ∇v -limited prescription is conceptually incomplete and that its results depend on the limit chosen. Most importantly, the power spectra calculated using this prescription contain substantial errors and the use of the more accurate PPM-RRM or MM-RRM scheme should be preferred.

8 COMPUTATIONAL ACCURACY AND EFFICIENCY

So far we have discussed four viable schemes to compute 21cm brightness temperatures in redshift space: the PPM-RRM scheme (Section 6.1.1), the MM-RRM scheme (Section 6.1.2), the linear μ_k -decomposition scheme (Section 5.3), and the DEMRF scheme (Section 6.4.3). To facilitate the usage of these schemes, we compare their usability, accuracy and efficiency in Table 1.

With N-body particle data (numerical simulation), the PPM-RRM scheme has no ambiguity in finding new particle locations in redshift space. When particle data is re-smoothed onto a redshift-space grid four times finer than RT grid resolution, PPM-RRM ($4 \times \text{RT}$) can accurately compute the power spectrum down to the RT resolution scale. However, the scheme is very computationally expensive and difficult to code, so we recommend to use it only as a development tool and for benchmarking, not for production work.

The MM-RRM ($4 \times \text{RT}$) scheme is the perfect tool for production work. It requires only 1/6 of total computational effort of the PPM-RRM ($4 \times \text{RT}$) scheme (including preliminary calculations), and the results are just as accurate. Using the fine ($4 \times \text{RT}$), instead of coarse (RT) grid does not really add to the total computational

distribution of $(1 + \delta_{\rho_{\text{HI}}}(\mathbf{r})) / |1 + \delta_{\partial_r v}(\mathbf{r})|$ has 1 as the mean in redshift space.

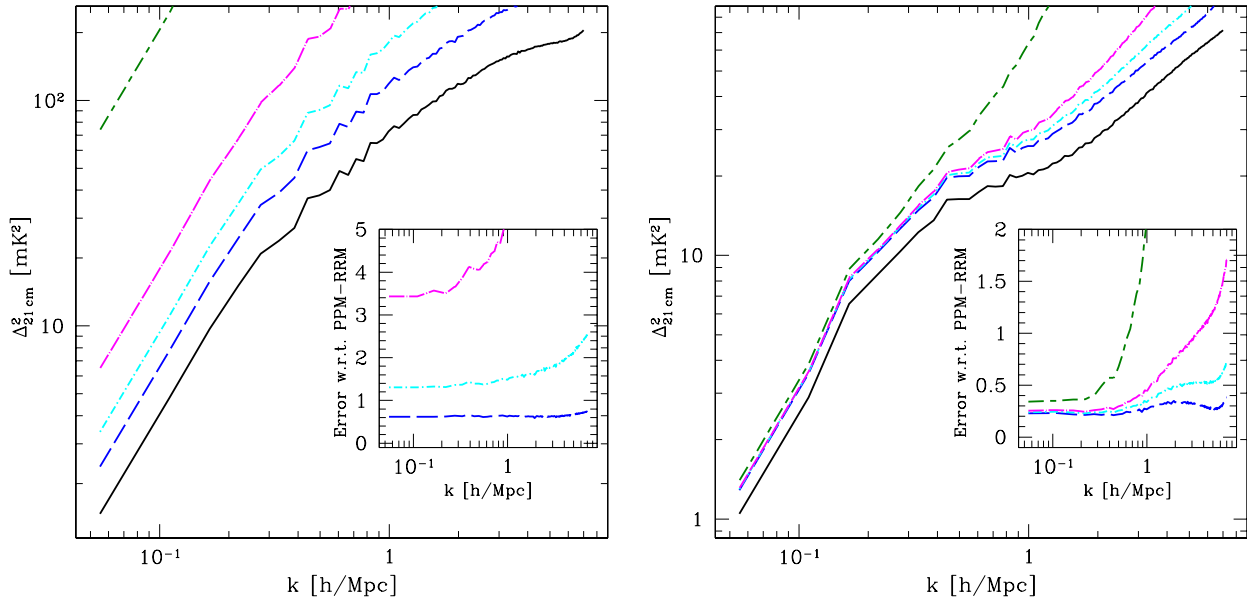


Figure 10. Power spectra of 21cm brightness temperature at 50% ionized epoch ($z = 9.457$). We show the results of the ∇v -limited prescription with the cap $\langle \delta_{\partial_r v} \rangle_{\text{cell}} \geq -\lambda$ at $\lambda = 0.5$ (long-dashed, blue), 0.7 (dot-short-dashed, cyan), 0.9 (dot-long-dashed, magenta), and 0.99 (short-dash-long-dashed, dark green), compared to the results of the PPM-RRM (4 \times RT) scheme (solid, black). The fractional errors of the ∇v -limited prescription are with respect to the PPM-RRM (4 \times RT) result, plotted in the inset. Left panel: assuming a fully neutral Universe ($x_{\text{HI}} = 1$); right panel: using the actual reionization fluctuations from the simulation.

effort. Note also that it can be directly used for semi-numerical simulations that evolve density on grids and do not use particles.

The DEMRF scheme is a nicely posed scheme since it is just a mathematical integration. However, in practise if we wish to substitute the cell-wise average $\langle \exp \left[-i \left(\frac{1+z_{\text{cos}}}{H(z_{\text{cos}})} \right) k_{\parallel} v_{\parallel}(\mathbf{r}) \right] \rangle_{\text{cell}}$ with $\exp \left[-i \left(\frac{1+z_{\text{cos}}}{H(z_{\text{cos}})} \right) k_{\parallel} \langle v_{\parallel}(\mathbf{r}) \rangle_{\text{cell}} \right]$ using cell-wise velocity, this scheme loses accuracy at the cell size $\sim 114/1024 \approx 0.11$ Mpc/h. Moreover, the DEMRF (2 \times RT) scheme is neither the most accurate nor the most efficient, so it is not to be recommended for production work. However, it is useful for validating the results from the PPM-RRM and MM-RRM schemes.

In the case of no realization, one can employ the linear μ_k -decomposition scheme which yields the redshift-space power spectrum with moderate accuracy and the least computational effort. It also has as a useful feature that it can proceed with only real-space statistics as input, making it an ideal tool for pure analytical modeling, and as such it has been used by many authors (e.g. Pritchard & Furlanetto 2007).

The upshot is that we recommend the MM-RRM (4 \times RT) scheme for practical usage, and the PPM-RRM (4 \times RT) for development.

9 CONCLUSIONS

- We have demonstrated that the neglect of peculiar velocity introduces a substantial error in 21cm brightness temperature spectra from the EOR and noticeable anisotropy in the 21cm power spectrum. We did this in three different ways: first, we compared the 3D power spectra computed uncorrected for peculiar velocity (UPV scheme), from the linear μ_k -decomposition scheme, and from a particle-based numerical scheme (PPM-RRM); second, we com-

pared the 21cm brightness temperature spectra computed from the UPV scheme and the PPM-RRM scheme, along 5 different sight-lines; lastly, we compared the angle-averaged 21cm power spectra computed from the linear μ_k -decomposition scheme and the UPV scheme, respectively. The non-trivial difference between results with and without peculiar velocity correction motivates our thorough investigation here of the effect of peculiar velocity on 21cm signal as well as more careful treatment of this effect on reionization simulation data than previously made.

- We clarify that peculiar velocity distorts the mapping of 21cm brightness temperature not only by shifting the apparent location in redshift-space, but also by modifying the brightness temperature itself in real-space. We show that the combined effect, which we call “21cm redshift-space distortion”, establishes, in the limit of low optical depth and high spin temperature, the exact proportionality between observed 21cm brightness temperature and the neutral hydrogen density as measured in redshift-space. This proportionality makes it possible to infer the three-dimensional distribution of neutral hydrogen density using 21cm brightness temperature measurements.

- We show that this proportionality between 21cm observed brightness temperature and the redshift-space neutral hydrogen density, however, can break down when $\tau_{21\text{cm}} \gtrsim 1$ and/or $T_s \lesssim T_{\text{CMB}}$. For the first case, we check the optically thin approximation, and demonstrate that this widely-assumed approximation is mostly valid in the IGM, but it can be invalid in some cases, e.g. in virialized halos where the peculiar velocity gradient can be large enough to cancel the Hubble flow. For the second case, we show that the proportionality mentioned above is spoiled by the spatially-varying T_s -dependent factor $1 - T_{\text{CMB}}/T_s^{r, \text{eff}}(\mathbf{r})$. This $T_s^{r, \text{eff}}(\mathbf{r})$ includes a correction to T_s of the order v/c due to peculiar velocity.

- In the optically-thick regions, a divergence of 21cm bright-

Table 1. Usability, accuracy and efficiency of various computational schemes for the redshift-space brightness temperature. Our simulation is in a box with 114 Mpc/h on each side, has 3072^3 N-body particles, and evolves reionization on a 256^3 RT grid.

	PPM-RRM		MM-RRM			DEMRF		Linear $\mu_{\mathbf{k}}$ -decomp.
	1×RT	4×RT	1×RT	2×RT	4×RT	1×RT	2×RT	4×RT
Input data type	N-body particle (\mathbf{x}, \mathbf{v}) (3072^3 particles), and RT grid x_i (256^3 grid size)		Cell-wise (\mathbf{x}, \mathbf{v}) in 256^3 , 512^3 , and 1024^3 grid size (1×, 2× and 4×RT, respectively), and RT grid x_i (256^3 grid size)			Cell-wise (\mathbf{x}, \mathbf{v}) in 256^3 and 512^3 grids (1× and 2×, respectively), and RT grid x_i (256^3 grid)		Cell-wise (\mathbf{x}, \mathbf{v}) in 1024^3 grid size, and RT grid x_i (256^3 grid size), or real-space power spectra directly
Output data type	HI density in redshift-space grid in 256^3 and 1024^3 grid size (1× and 4×RT, respectively)		HI density in redshift-space grid in 256^3 , 512^3 , and 1024^3 grid size (1×, 2× and 4×RT, respectively)			Power spectrum only ^a		Power spectrum only
Usability	Numerical simulations		Numerical or semi-numerical simulations			Numerical or semi-numerical simulations		Analytical modeling (no realization), numerical or semi-numerical simulations
Well defined	Yes		Inaccurate assumptions on small scales			Unable to use on a grid too fine (see Section 6.4.3)		Yes
Accuracy ^b in 1D power spectrum	at $k \leq 2$ h/Mpc	$\lesssim 2\%$ benchmark	$\lesssim 4\%$	$\lesssim 2\%$	0%	$\lesssim 1\%$	0%	$\lesssim 10\%$
	at $2 < k < 7$ h/Mpc	$\lesssim 20\%$ benchmark	$\lesssim 40\%$	$\lesssim 20\%$	$\lesssim 1\%$	$\lesssim 14\%$	$\lesssim 5\%$	$\lesssim 10\%$
SUs (=cores × hours)	Preliminary ^c	0	350	358	375	350	358	375
	Processing	2048	0.1	0.7	8.5	52	887	5.3
	Total	2048	350	359	384	402	1245	380

^a In principle, a brightness temperature data cube in redshift space can be constructed by taking the inverse Fourier transform of the \mathbf{k} -space brightness temperature evaluated using Eqns. (56) and (58) for the DEMRF scheme and linear $\mu_{\mathbf{k}}$ -decomposition scheme, respectively. However, aliasing effects from multiple forward and backward FFTs can introduce errors. It is beyond the scope of this paper to test these effects.

^b All errors here are with respect to the results from the PPM-RRM (4×RT) scheme, which is the most accurate.

^c Preliminary SUs for the MM-RRM scheme, linear $\mu_{\mathbf{k}}$ -decomposition scheme, and DEMRF scheme refers to the SUs used to smooth particle density and velocity data onto a regular, real-space, grid.

ness temperature can result from naively applying the commonly-employed formula of 21cm brightness temperature which is, however, only valid in the optically-thin limit. We show that, in the optically thick limit, the optical depth can depend upon higher order spatial derivatives of peculiar velocity than $dv_{\parallel}/dr_{\parallel}$.

- We clarify that it is the bulk velocity of the gas but not the thermal velocity that is responsible for the velocity correction to the optical depth and 21cm brightness temperature. This is done by showing that the latter constitutes only a negligible contribution to the correction, compared to the former, when $\tau_{21\text{cm}} \lesssim 1$.

- In the optically-thin limit, we derive the fully nonlinear Fourier transform of 21cm brightness temperature fluctuations as measured in redshift-space, in terms of the density, velocity, and ionization fields in real space, following the combined effect of 21cm redshift-space distortion. We further derive its power spectrum, assuming the density and velocity fluctuations are linear but the ionization field fluctuations can be nonlinear. This scheme, which we call the “linear $\mu_{\mathbf{k}}$ -decomposition scheme”, generalizes the linear theory previously considered in Barkana & Loeb (2005), which linearized the ionization field.

- To make careful treatment of the peculiar velocity effect on 21cm brightness temperature when using reionization simulation data, we propose and test two numerical schemes that compute the

21cm brightness temperature as measured in a redshift-space grid from real-space simulation data. Both schemes take advantage of the mapping from real- to redshift-space, one particle-based (PPM-RRM), and one grid-based (MM-RRM). We show that the MM-RRM scheme can be optimized to achieve the same high accuracy in the angle-averaged power spectrum as the PPM-RRM scheme, while being much more computationally efficient than the latter. If the RT grid resolution (on a mesh with Nyquist wavenumber $k_{N,RT}$, the mesh on which the ionization fluctuation field is determined) is coarser than the resolution of the density and peculiar velocity fields, we optimize the grid-based MM-RRM resolution by including all modes with $k \leq k_{N,RT}$ in a grid with Nyquist wavenumber $4k_{N,RT}$ which uses the finer-resolution density and velocity data, together with the coarser-resolution ionized fractions. This reduces the aliasing errors which would otherwise spoil the results for $k > k_{N,RT}/4$ if all data were coarsened to the RT-grid resolution. We show that this optimized MM-RRM scheme can compute the angle-averaged 21cm power spectrum within $\lesssim 1\%$ accuracy of the PPM-RRM(4×RT) results, for all modes $k \leq k_{N,RT}$.

- Our careful treatment of brightness temperature fluctuations in redshift space avoids the divergences that appear in the real-space evaluation when peculiar-velocity gradients are large. Such large gradients are a natural result of nonlinear structure formation on

small scales. We find that previous attempts to escape these divergences by numerically “clipping” the velocity gradients whenever they exceed some threshold (referred to here as the “ ∇v -limited prescription”) introduce significant errors in the 21cm power spectra on *all* scales, including scales much larger than that of the non-linearity.

- The upshot is that we provide an integrated understanding of how peculiar velocity affects 21cm tomography, and also an accurate and efficient numerical algorithm (MM-RRM) for practical numerical application.

- In this paper, we find that the fully nonlinear 21cm 1D power spectrum deviates from the 1D power spectrum in linear μ_k -decomposition scheme by roughly 10% at the 50% ionized epoch (see Section 6.4.2). The nonlinearity may introduce larger deviations when the 3D power spectrum is decomposed to extract only the $P_{\mu^A}(k)$ for cosmology. This nonlinear effect is interesting to explore, because the idea of using 21cm measurements for cosmology is based on the linear theory, and therefore it is essential to understand the nature of this nonlinear effect, and estimate its impact on 21cm cosmology. We will address these issues in the second paper of this series (Shapiro et al. 2011).

ACKNOWLEDGMENTS

The authors wish to thank Marcelo Alvarez, Kanan Datta, Leon Koopmans, Matthew McQuinn, Ue-Li Pen, Mario Santos, Max Tegmark, and Jun Zhang for useful discussions. YM is deeply indebted to Eiichiro Komatsu and Donghui Jeong for enlightening discussions on the redshift space distortion in galaxy redshift surveys. YM and PRS would like to acknowledge the hospitality of the Aspen Center for Physics where part of this work was accomplished. The authors acknowledge the Texas Advanced Computing Center (TACC²⁴) at The University of Texas at Austin for providing HPC resources, under NSF TeraGrid grants tg-ast0900005 and TG-080028N and TACC internal allocation grant “A-asoz”, as well as the Swedish National Infrastructure for Computing (SNIC) resources at HPC2N (Umeå, Sweden), which have contributed to the research results reported within this paper. This work was supported in part by Swiss National Science Foundation grant 200021-116696/1, NSF grants AST-0708176 and AST-1009799, NASA grants NNX07AH09G, NNG04G177G and NNX11AE09G, Chandra grant SAO TM8-9009X, and Swedish Research Council grant 2009-4088. ITI was supported by The Southeast Physics Network (SEPNet) and the Science and Technology Facilities Council grant number ST/F002858/1. KA is supported in part by Basic Science Research Program through the National Research Foundation of Korea (NRF) funded by the Ministry of Education, Science and Technology (MEST; 2009-0068141, 2009-0076868) and by KICOS through K20702020016-07E0200-01610 funded by MOST.

REFERENCES

Adshead, P., Easther, R., Pritchard, J., and Loeb, A., 2011, JCAP, 2, 21
 Alvarez, M. A., Busha, M., Abel, T., and Wechsler, R. H., 2009, ApJL, 703, L167
 Baek, S., Semelin, B., Di Matteo, P., Revaz, Y., & Combes, F., 2010, A & A, 523, A4

Barger, V., Gao, Y., Mao, Y., & Marfatia, D., 2009, Phys. Lett. B 673, 173
 Barkana, R., & Loeb, A., 2005, ApJL, 624, L65
 Barkana, R., & Loeb, A., 2006, MNRAS Lett., 372, L43
 Bharadwaj, S., Nath, B. B., & Sethi, S. K., JApA, 2001, 22, 21
 Bharadwaj, S. & Ali, S., 2004, MNRAS, 352, 142
 Bowman, J. D., Morales, M. F., & Hewitt, J. N., 2008, ApJ, 661, 1
 Chen, X. & Miralda-Escudé, J., 2004, ApJ, 602, 1
 Chuzhoy, L., & Shapiro, P. R., 2006, ApJ, 651, 1
 Ciardi, B. & Madau, P., 2003, ApJ, 596, 1
 Cui, W., Liu, L., Yang, X., Wang, Y., Feng, L., and Springel, V., 2008, ApJ, 687, 738
 Friedrich, M. M., Mellema, G., Alvarez, M. A., Shapiro, P. R., and Iliev, I. T., 2010, arXiv1006.2016
 Furlanetto, S. R., Zaldarriaga, M., and Hernquist, L., 2004, ApJ, 613, 1
 Gnedin, N. Y. & Ostriker, J. P., 1997, ApJ, 486, 581
 Iliev, I. T., Mellema, G., Pen, U.-L., Merz, H., Shapiro, P. R., & Alvarez, M. A., 2006, MNRAS, 369, 1625
 Iliev, I. T., Mellema, G., Shapiro, P. R., Mao, Y., Koda, J., & Ahn, K., 2011, *in preparation*
 Iliev, I. T., Shapiro, P. R., Ferrara, A., and Martel, H., 2002, ApJL, 572, L123
 Iliev, I. T., Mellema, G., Pen, U.-L., Bond, J. R., & Shapiro, P. R., 2008a, MNRAS, 384, 863
 Iliev, I. T., Shapiro, P. R., Mellema, G., Merz, H., & Pen, U.-L., 2008b, TeraGrid08 proceedings, arXiv:0806.2887.
 Jing, Y. P., 2005, ApJ, 620, 559
 Kaiser, N., 1987, MNRAS, 227, 1
 Komatsu, E., et al. [WMAP Collaboration], 2011, ApJS, 192, 18
 Lidz, A., Zahn, O., McQuinn, M., Zaldarriaga, M., & Dutta, S., 2007, ApJ, 659, 865
 Mao, Y., Tegmark, M., McQuinn, M., Zaldarriaga, M., & Zahn, O., 2008 Phys. Rev. D, 78, 023529
 Mao, Y., Shapiro, P. R., Iliev, I. T., Mellema, G., Koda, J., & Pen, U.-L., 2010, ASP Conference Series Vol. 432, 212
 McQuinn, M., Lidz, A., Zahn, O., Dutta, S., Hernquist, L., & Zaldarriaga, M., 2007, MNRAS, 377, 1043
 McQuinn, M., Zahn, O., Zaldarriaga, M., Hernquist, L., & Furlanetto, S. R., 2006, ApJ, 653, 815
 Mellema, G., Iliev, I. T., Alvarez, M. A., & Shapiro, P. R., 2006a New Astronomy, 11, 374
 Mellema, G., Iliev, I. T., Pen, U.-L. & Shapiro, P. R., 2006b, MNRAS, 372, 679
 Mesinger, A., Furlanetto, S., and Cen, R., 2011, MNRAS, 411, 955
 Mihalas, D., 1978, Stellar Atmospheres (2nd ed.), W. H. Freeman and Co., pp.495-496
 Paciga, G., Chang, T.-C., Gupta, Y., Nityanada, R., Odegova, J., Pen, U.-L., Peterson, J., Roy, J., and Sigurdson, K., 2010, ArXiv: 1006.1351
 Pritchard, J. R., & Furlanetto, S. R., 2007, MNRAS, 376, 1680
 Santos, M. G. & Cooray, A., 2006, Phys. Rev. D 74, 083517
 Santos, M. G., Ferramacho, L., Silva, M. B., Amblard, A., and Cooray, A., 2010, MNRAS, 406, 2421
 Shapiro, P. R., Ahn, K., Alvarez, M. A., Iliev, I. T., Martel, H., & Ryu, D., 2006, ApJ, 646, 681
 Shapiro, P. R., Iliev, I. T., Mellema, G., Pen, U.-L., & Merz, H., 2008, American Institute of Physics Conference Series, Vol.1035
 Shapiro, P. R., Mao, Y., Iliev, I. T., Mellema, G., Koda, J., and Ahn, K., 2011, *in preparation*

²⁴ <http://www.tacc.utexas.edu>

Shapiro, P. R., Martel, H., Villumsen, J. V., & Owen, J. M., 1996, ApJS, 103, 269

Shaw J. R. & Lewis A., 2008, Phys. Rev. D 78, 103512

Tegmark, M., and Zaldarriaga, M., 2009, Phys. Rev. D 79, 083530

Tegmark, M., and Zaldarriaga, M., 2010, Phys. Rev. D 82, 103501

Thomas, R. M., Zaroubi, S., Ciardi, B., Pawlik, A. H., Labropoulos, P., Jelić, V., Bernardi, G., Brentjens, M. A., de Bruyn, A. G., Harker, G. J. A., Koopmans, L. V. E., Mellema, G., Pandey, V. N., Schaye, J., and Yatawatta, S., 2009, MNRAS, 393, 32

Trac, H., & Cen, R., 2007, ApJ, 671, 1

Visbal, E., Loeb, A., and Wyithe, S., 2009, JCAP, 10, 30

Wang X., Hu W., 2006, ApJ, 643, 585

Wise, J. H. & Abel, T., 2010, arXiv:1012.2865

Wyithe, S., Loeb, A., and Geil, P., 2008, MNRAS, 383, 1195

Zahn, O., Lidz, A., McQuinn, M., Dutta, S., Hernquist, L., Zaldarriaga, M., and Furlanetto, S. R., 2007, ApJ, 654, 12

Zahn, O., Mesinger, A., McQuinn, M., Trac, H., Cen, R., and Hernquist, L. E., 2010, arXiv:1003.3455

Zhang, J., Hui, L., & Haiman, Z., 2007, MNRAS, 375, 324

APPENDIX A: SPH-LIKE SMOOTHING WITH ADAPTIVE KERNEL

In this section, we briefly describe the SPH-like technique to smooth N-body particle data onto a grid. We refer readers to Shapiro et al. (1996) for a comprehensive discussion of smooth particle hydrodynamics with an adaptive kernel.

Assume that the continuous density and velocity fields are represented by N_p particles with mass m_i , location \mathbf{r}_i , and velocity \mathbf{v}_i ($i = 1, \dots, N_p$). We define a particle's kernel h_i to be the distance between the particle i and its 32nd nearest neighbor particle. We take the “scatter” approach to smooth particle data (see Fig. 2 of Shapiro et al. 1996 for an illustration of the *scatter* vs. *gather* approaches), i.e., a field point at \mathbf{r} is influenced by a particle i if this particle's *own* influence zone covers this field point (e.g., in the case of isotropic kernel, $|\mathbf{r} - \mathbf{r}_i| \leq h_i$).

We employ the triangular kernel function with adaptive kernel size h , $W(\mathbf{r}; h) = f_h(x)f_h(y)f_h(z)$, centered at the particle location to smooth its data. The function $f_h(x)$ is triangular-shaped with width $2h$, i.e.,

$$f_h(x) = \begin{cases} -\frac{x}{h^2} + \frac{1}{h} & , \quad 0 \leq x \leq h \\ \frac{x}{h^2} + \frac{1}{h} & , \quad -h \leq x < 0 \\ 0 & , \quad \text{otherwise} \end{cases} \quad (\text{A1})$$

Smoothed Fields at a Point

The smoothed mass density and momentum density fields are defined, respectively, by

$$\rho(\mathbf{r}) = \sum_i m_i W(\mathbf{r} - \mathbf{r}_i; h_i), \quad (\text{A2})$$

$$\mathcal{P}(\mathbf{r}) = \sum_i m_i \mathbf{v}_i W(\mathbf{r} - \mathbf{r}_i; h_i). \quad (\text{A3})$$

To preserve momentum, the continuous velocity field is defined by

$$\mathbf{v}(\mathbf{r}) = \mathcal{P}(\mathbf{r})/\rho(\mathbf{r}). \quad (\text{A4})$$

We identify the bulk-flow velocity of the IGM at a particle's position \mathbf{r}_i to be the smooth field $\mathbf{v}(\mathbf{r}_i)$ evaluated at \mathbf{r}_i .

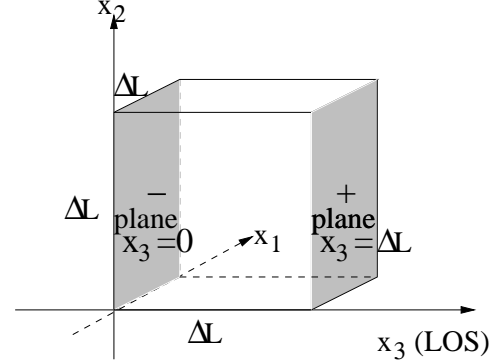


Figure A1. Cartoon of computing $\langle dv_{\parallel}/dr_{\parallel} \rangle_{\text{cell}}$ for a cubical cell of size ΔL on each side. In this cartoon, we assume the LOS along the x_3 -axis, then the “+ plane” (“- plane”) is the x_1 - x_2 plane with $x_3 = \Delta L$ ($x = 0$).

Smoothed Fields of a Cell

To smooth particle data onto a regular grid, we use the following approach to compute the cell-wise mass density,

$$\begin{aligned} \langle \rho \rangle_{\text{cell}} &= \frac{1}{V_{\text{cell}}} \int_{\text{cell}} \rho(\mathbf{r}) d^3 r \\ &= \frac{1}{V_{\text{cell}}} \sum_i m_i \int_{\text{cell}} W(\mathbf{r} - \mathbf{r}_i; h_i) d^3 r, \end{aligned} \quad (\text{A5})$$

where the integral $\int_{\text{cell}} W(\mathbf{r} - \mathbf{r}_i; h_i) d^3 r$ can be evaluated analytically, and is only a function of h_i and the relative location between the particle i and the cell boundaries. Similarly, the cell-wise momentum density is

$$\begin{aligned} \langle \mathcal{P} \rangle_{\text{cell}} &= \frac{1}{V_{\text{cell}}} \int_{\text{cell}} \mathcal{P}(\mathbf{r}) d^3 r \\ &= \frac{1}{V_{\text{cell}}} \sum_i m_i \mathbf{v}_i \int_{\text{cell}} W(\mathbf{r} - \mathbf{r}_i; h_i) d^3 r. \end{aligned} \quad (\text{A6})$$

The cell-wise velocity is defined in a momentum-preserving way,

$$\langle \mathbf{v} \rangle_{\text{cell}} = \langle \mathcal{P} \rangle_{\text{cell}} / \langle \rho \rangle_{\text{cell}}. \quad (\text{A7})$$

$d\mathbf{v}_{\parallel}/d\mathbf{r}_{\parallel}$ of a Cell

We compute the cell-wise velocity gradient $\langle dv_{\parallel}/dr_{\parallel} \rangle_{\text{cell}}$ in the following way (assuming the LOS is along one of the principal axes of a cubical cell),

$$\begin{aligned} \langle dv_{\parallel}/dr_{\parallel} \rangle_{\text{cell}} &= \frac{1}{V_{\text{cell}}} \int_{\text{cell}} \frac{dv_{\parallel}}{dr_{\parallel}}(\mathbf{r}) d^3 r \\ &= \frac{1}{\Delta L} \left[\langle v_{\parallel} \rangle_{+\text{plane}} - \langle v_{\parallel} \rangle_{-\text{plane}} \right], \end{aligned} \quad (\text{A8})$$

where ΔL is the size of the cubical cell, “+ plane” (“- plane”) is the cell wall perpendicular to the LOS with larger (smaller) location along the r_{\parallel} -axis, and $\langle v_{\parallel} \rangle_{+\text{plane}}$ is the velocity mean on the “+” cell wall, i.e. $\langle v_{\parallel} \rangle_{+\text{plane}} = \frac{1}{(\Delta L)^2} \int_{+\text{plane}} d^2 r_{\perp} v_{\parallel}(\vec{S}_{\perp}, +\text{plane})$. Unfortunately, we cannot apply the same smoothing as in Eqn. (A5) to compute the velocity average, because the velocity defined in Eqn. (A4) involves a summation in the denominator.

To circumvent this, we approximate the smoothed velocity averaging on a cell wall by the momentum-preserving velocity, i.e.

$$\langle v_{\parallel} \rangle_{\text{plane}} \rightarrow \langle \mathcal{P}_{\parallel} \rangle_{\text{plane}} / \langle \rho \rangle_{\text{plane}}, \quad (\text{A9})$$

where the r.h.s. is the center-of-mass velocity of a thin layer on the cell wall. The surface mass density of the cell wall is

$$\begin{aligned} \langle \rho \rangle_{\text{plane}} &= \frac{1}{(\Delta L)^2} \int_{\text{plane}} \rho(\mathbf{r}) d^2 r_{\perp} \\ &= \frac{1}{(\Delta L)^2} \sum_i m_i \int_{\text{plane}} W(\mathbf{r} - \mathbf{r}_i; h_i) d^2 r_{\perp}, \quad (\text{A10}) \end{aligned}$$

where the integral can be evaluated analytically,

$$\begin{aligned} \int_{\text{plane}} W(\mathbf{r} - \mathbf{r}_i; h_i) d^2 r_{\perp} &= \left[\int_{x_{1,c}-\Delta L/2}^{x_{1,c}+\Delta L/2} f_{h_i}(x_1 - x_{1,i}) dx_1 \right] \\ &\times \left[\int_{x_{2,c}-\Delta L/2}^{x_{2,c}+\Delta L/2} f_{h_i}(x_2 - x_{2,i}) dx_2 \right] \times f_{h_i}(x_{3,\text{plane}} - x_{3,i}). \quad (\text{A11}) \end{aligned}$$

Here we take x_1 and x_2 to be axes in the cell wall perpendicular to the LOS axis x_3 , $x_{3,\text{plane}}$ is the LOS coordinate of the cell wall, $x_{1,c}$ and $x_{2,c}$ are the transverse coordinates of the center of the cell, and \mathbf{x}_i are the three-dimensional coordinates of the particle i .

Similarly, we use

$$\begin{aligned} \langle \mathcal{P}_{\parallel} \rangle_{\text{plane}} &= \frac{1}{(\Delta L)^2} \int_{\text{plane}} \mathcal{P}_{\parallel}(\mathbf{r}) d^2 r_{\perp} \\ &= \frac{1}{(\Delta L)^2} \sum_i m_i v_{i,\parallel} \int_{\text{plane}} W(\mathbf{r} - \mathbf{r}_i; h_i) d^2 r_{\perp}. \end{aligned}$$